

MIT Open Access Articles

Oxidation and pyrolysis of methyl propyl ether

The MIT Faculty has made this article openly available. **Please share** how this access benefits you. Your story matters.

Citation: Johnson, Matthew S., Nimlos, Mark R., Ninnemann, Erik, Laich, Andrew, Fioroni, Gina M. et al. 2021. "Oxidation and pyrolysis of methyl propyl ether." *International Journal of Chemical Kinetics*, 53 (8).

As Published: <http://dx.doi.org/10.1002/kin.21489>

Publisher: Wiley

Persistent URL: <https://hdl.handle.net/1721.1/140517>

Version: Author's final manuscript: final author's manuscript post peer review, without publisher's formatting or copy editing

Terms of use: Creative Commons Attribution-Noncommercial-Share Alike



Oxidation and Pyrolysis of Methyl Propyl Ether

Matthew S. Johnson,[†] Mark R. Nimlos,[‡] Erik Ninnemann,[¶] Andrew Laich,[¶]
Gina M. Fioroni,[‡] Dongil Kang,[§] Lintao Bu,[‡] Duminda Ranasinghe,[†] Sarah
Khanniche,[†] S. Scott Goldsborough,[§] Subith S. Vasu,[¶] and William H. Green^{*,†}

[†]*Department of Chemical Engineering, Massachusetts Institute of Technology, Cambridge,
MA 02139, United States*

[‡]*National Bioenergy Center, National Renewable Energy Laboratory, 15013 Denver West
Parkway, Golden, CO 80401-3393, USA*

[¶]*Center for Advanced Turbomachinery and Energy Research (CATER), Mechanical and
Aerospace Engineering, University of Central Florida, Orlando, FL 32816, USA*

[§]*Center for Transportation Research, Energy Systems Division, Argonne National
Laboratory, Argonne, IL 60439, USA*

E-mail: whgreen@mit.edu

Abstract

The ignition, oxidation, and pyrolysis chemistry of methyl propyl ether (MPE) was probed experimentally at several different conditions, and a comprehensive chemical kinetic model was constructed to help understand the observations, with many of the key parameters computed using quantum chemistry and transition state theory. Experiments were carried out in a shock tube measuring time variation of CO concentrations, in a flow tube measuring product concentrations, and in a rapid compression machine (RCM) measuring ignition delay times. The detailed reaction mechanism was constructed using the Reaction Mechanism Generator software. Sensitivity and flux analyses were used to identify key rate and thermochemical parameters, which were

then computed using quantum chemistry to improve the mechanism. Validation of the final model against the 1–20 bar 600–1500 K experimental data is presented with a discussion of the kinetics. The model is in excellent agreement with most of the shock tube and RCM data. Strong non-monotonic variation in conversion and product distribution is observed in the flow-tube experiments as the temperature is increased, and unusually strong pressure-dependence and significant heat release during the compression stroke is observed in the RCM experiments. These observations are largely explained by a close competition between radical decomposition and addition to O₂ at different sites in MPE, this causes small shifts in conditions to lead to big shifts in the dominant reaction pathways. The validated mechanism was used to study the chemistry occurring during ignition in a diesel engine, simulated using Ignition Quality Test (IQT) conditions. At the IQT conditions, where the MPE concentration is higher, bimolecular reactions of peroxy radicals are much more important than in the RCM.

1 Introduction

When mixed with diesel fuels oxygenated species tend to reduce soot formation in engines [1–3]. Ethers in particular accomplish this goal while also enhancing cetane numbers and allowing the use of less expensive diesel [4]. Ether cetane numbers, however, can fall within a wide range of values from 55 to 110 [4]. Unfortunately, our understanding of ether combustion mechanisms is incomplete making it difficult to predict the impact particular ethers might have on the cetane number of diesel.

Dimethyl ether has been fairly well studied across a wide temperature range [5–10]. However the chemistry of larger ethers is much less understood. Several studies have looked specifically at ethyl methyl ether, methyl tertiary butyl ether, ethyl tertiary butyl ether and diethyl ether [11–14]. However, these studies focused primarily on high temperature ranges. A number of other studies have focused on how these compounds might act as octane enhancers [15–17].

In this study we investigate the detailed chemistry of methyl propyl ether over a wide range of temperatures. Methyl propyl ether has a long enough alkyl chain to undergo the radical feedback loops typical of low temperature alkane combustion. It is also small enough to allow construction of a highly detailed mechanism.

2 Methods

2.1 Shock Tube

2.1.1 Experimental Setup

Experiments were performed at the University of Central Florida’s shock tube facility with two different MPE mixtures, one for oxidation and the other for pyrolysis experiments. Only a brief description of the shock tube is presented, as more details of the procedure and instrumentation for this shock tube can be found in earlier studies [18, 19]. The oxidation mixture consisted of 0.1% MPE at an equivalence ratio of 1, and the pyrolysis mixture consisted of 0.5% MPE; both mixtures were balanced in argon. Carbon monoxide (CO) time-histories were measured for both mixtures with reflected shock conditions of 1205–1511 K and 8.41–9.69 atm.

2.1.2 Shock Tube Facility

The shock tube facility at the University of Central Florida (UCF) has an inner diameter of 14.17 cm and can accommodate polycarbonate or metal diaphragms in either a single or stacked arrangement. A scored, single polycarbonate diaphragm that separated the driver and driven sections was ruptured at a known pressure to initiate the incident normal shock-wave. For measuring the incident shock velocity, there were five time-of-arrival PCB 113B26 pressure transducers connected to four Agilent 53220A timer-counters. This velocity was then extrapolated to the end wall for use in 1D ideal shock relations to calculate the temperature (T_5) and pressure (p_5) behind the reflected shock. Before each experiment, the

entire shock tube was vacuumed down to a rough level with Agilent DS 102 rotary vane pumps. This was followed by further vacuuming the driven section with an Agilent V301 turbo-molecular pump to achieve a vacuum of 10–5 Torr or better in less than 1 h. Oxidation and pyrolysis mixtures were prepared manometrically in a 33 L stainless steel mixing tank that was fitted with a magnetically driven stirrer. To ensure mixture homogeneity, a 1 h minimum mixing time was allotted. Ultra high purity (99.999%) argon and oxygen were supplied by nexAir, and MPE was supplied by Sigma Aldrich with a purity of 97%. Industrial grade (99.998%) helium or nitrogen, or some composition of the two were used as the driver gas for these experiments.

2.1.3 Shock Tube Diagnostics

Diagnostics used for these experiments included a pressure transducer and a fixed-wavelength direct absorption laser setup at the test location 2 cm from the end wall. Reflected shock pressure was measured with a side wall mounted Kistler 603B1 pressure transducer with an applied RTV coating, while time resolved concentration measurements of CO were made using a continuous wave distributed feedback quantum cascade laser (CW-DFBQCL) supplied by Alpes Lasers. This laser was centered at 2046.30 cm^{-1} targeting the P(23) transition of CO, which provided a strong absorption feature and enabled interference-free measurements. A schematic of this optical setup is shown in Fig. 1. The wavelength was verified before each experiment with a Bristol 771 wavemeter. Two detectors supplied by Vigo (PIV-4TE-5-2 x 2) were used to measure the intensity of focused laser light for calculations in determining the absorbance of the laser beam during experiments. The absorbance is related to mole fraction and measured laser intensities by the Beer-Lambert Law, given in Eq. 1, where I_{trans} and I_{ref} are laser intensities passing through the shock tube during the experiment and under vacuum, respectively. σ is the absorption cross section, p_5 is the reflected shock pressure, R is the universal gas constant, X_{CO} is the CO mole fraction, and L is the optical

path length.

$$\alpha = -\ln \frac{I_{trans}}{I_{ref}} = \sigma_{CO}(\nu, T, P) \frac{p_5}{RT_5} X_{CO} L \quad (1)$$

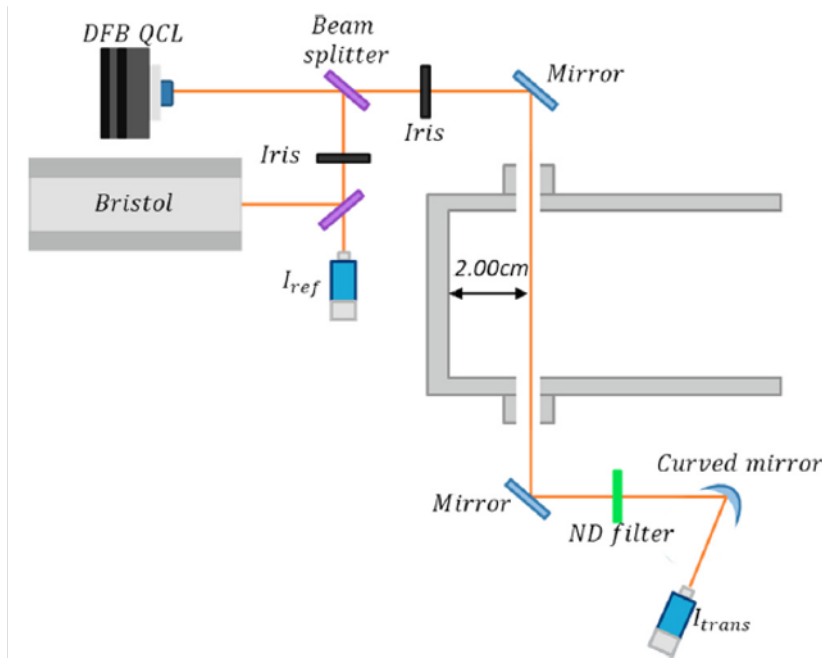


Figure 1: Schematic of shock tube and laser setup used to perform CO time-history measurements.

2.2 Flow Tube

Flow reactor experiments were carried out in a straight quartz flow tube that is 1" in diameter and 30" in length at the National Renewable Energy Laboratory facility in Golden, Colorado [20, 21]. The flow tube is heated in a ceramic furnace with a 28" heated zone. Helium dilution gas, fuel, and air are introduced at the inlet of the reactor and the effluent is directly sampled at the outlet via an inert gas sampling line directly to two gas chromatography (GC) systems. The inert gas sampling line is positioned in the middle of the flow tube exit at a depth of 0.5" and is maintained at 75°C in order to avoid condensation of components inside the transfer line. Liquid fuel was introduced at 0.5 mol% and an excess of oxygen was used at 9.5 mol%. Helium was used as the dilution gas and the flow rate was adjusted to

maintain a constant residence time of two and five seconds throughout the temperature range investigated (700 K–900 K). The first GC contains two 60m x 0.32 mm x 1 m DB-1 (Agilent Technologies) columns. One is connected to a mass spectrometer for the identification of compounds in the four carbon or greater range, the second is connected to a flame ionization detector for quantitation. The second GC is equipped with three columns and detectors for analysis of the light molecular weight compounds. A Rt Alumina bond (Restek) 30m x 0.32 mm x 5 m column is connected to a flame ionization detector and is used to quantitate four carbon or fewer hydrocarbon compounds. A CP PoraBondQ (Varian) 50m x 0.32 mm x 5 m and a Rt Msieve 5A (Restek) 30 m x 0.53 mm x 50 m are connected to two separate thermal conductivity detectors and are used to quantitate carbon monoxide and dioxide respectively. Where available, pure components were used as standards purchased as custom mixtures (Matheson Specialty Gases) to calibrate the GCs for direct quantitation of combustion products, otherwise the method of effective carbon number was used where standards were not available [22]. The reactor is modeled as an isobaric isothermal ideal plug flow reactor, at $p=0.81$ atm (the ambient pressure at Golden, Colorado).

2.3 Quantum Chemistry and Rate Calculations

The G4 composite quantum chemistry method [23] was used to calculate energies of selected reactants, products and transition states in this study. This method uses geometries and vibrational frequencies calculated using DFT with B3LYP/6-31G(2df,p) and a series of single point calculations at different levels of theory with the highest being CCSD(T)/6-31G(d). The reported accuracy of the G4 technique was estimated by a comparison of calculated energies to experimental energies for the 454 species in the G3/05 test set, which showed that the average absolute deviation was $0.83 \frac{kcal}{mol}$. Transition states were confirmed to connect the reactants and products using the atomic motion of the single imaginary frequency and IRC calculations at the DFT level. The thermochemical and rate parameters were computed using the Rigid Rotor Harmonic Oscillator (RRHO) method with 1D hindered rotors and

tunneling corrections.

2.4 Rapid Compression Machine

Argonne National Laboratory’s twin-piston rapid compression machine (tpRCM) was used to acquire autoignition data for MPE at elevated temperatures and pressures. A detailed overview of the configuration and recent modifications to the tpRCM, as well as uncertainties associated with experimental measurements can be found in, and are briefly described here [24]. The tpRCM, which can be operated as single-, or two-piston actuation, is pneumatically-driven and hydraulically controlled. A ring-groove arrangement in the hydraulic chambers at the end of the stroke facilitates deceleration, while the hydraulic chambers are pressurized during the test period to minimize piston rebound at ignition. The reaction chamber has a 50.8 mm bore with a clearance height at maximum compression of ~ 25.5 mm; the volumetric compression ratio is near 12.1:1 for two-piston operation, and near 6.4:1 when only one piston is actuated. The reaction chamber pistons incorporate crevices machined around their circumference to suppress vorticular motion during, and post-compression [25]. The robustness of the configuration for the current study was verified as suggested by Bourgeois et al. 2018 [26]. The exterior of the reaction chamber is heated using a combination of band, tape and cartridge heaters, with high density insulation fitted between the flanges of the cylinders and the hydraulic chamber. Thermal uniformity of 0.2% is achieved in the axial and azimuthal directions across the interior and exterior surfaces. The dynamic pressure is measured using a Kistler 6045A-U20 transducer, regularly calibrated to 250 bar, and coupled to a Kistler 5064 charge amplifier. The 6045A-U20 is designed for thermal shock resistance ($< \pm 1\%$), and incorporates a reinforced diaphragm for knock protection. The signal is recorded with a NI 9239 (24-bit/50kHz) data acquisition card. A Savitzky-Golay algorithm with 2nd-order fit is applied to condition the recorded signals with a window of 0.25 ms. A 5.6 L stainless steel tank, heated to $\sim 70^\circ$ C, is used to prepare the fuel, diluent (Ar and N₂), and O₂ mixtures. Liquid fuel at room temperature is

first injected into the evacuated tank through a septum, and then the high purity gases are supplied in the sequence of Ar (99.9997%, Airgas), N₂ (99.9998%, Airgas) and O₂ (99.9997%, Airgas). After introduction, the mixture is allowed to diffusively mix for a minimum of 45 minutes before beginning the tests. The evaporation efficiency of each test fuel is calculated from ideal gas relationships, with $\sim 100\%$ typically achieved, while the mass of fuel and partial pressure of gaseous components are used to determine the molar composition of the mixture. The compressed temperatures, ignition delay times and heat release rates are determined by post-processing recorded pressure traces. To accurately extract these, equivalent non-reacting tests are conducted at each condition where the O₂ is replaced by N₂ since these have very similar thermophysical properties; the non-reactive and reactive traces are aligned at 40% of the pressure rise. This is necessary since many test conditions with these mixtures yield preliminary exothermicity (e.g., low-temperature/first-stage heat release) before the end of piston compression. Figure 2a illustrates representative pressure-time histories where the end of compression time (t_0), first-stage (τ_1) and main ignition times (τ) are identified. Note there are two pressure records for each test point, where excellent shot-to-shot repeatability is demonstrated. Estimates of uncertainty and statistical (i.e., month-to-month) variations in the measurements are about $\pm 10\%$ for ignition time. The non-reactive tests are also used to derive effective volume-time histories for chemical kinetic modeling where the rates of compression heating and pressure/temperature decay due to heat loss during the induction period can be reasonably taken into account [27]. The compressed temperatures (T_C 's) are calculated using the adiabatic core hypothesis:

$$\int_{T_i}^{T_c} \frac{\gamma}{\gamma - 1} \frac{dT}{T} = \ln \frac{p_c}{p_i} \quad (2)$$

where the subscripts i and c indicate the initial and compressed conditions, respectively, while γ is the ratio of specific heats of the gas mixture. Non-reactive mixtures are used to estimate the T_C 's. An uncertainty analysis associated with ANL's tpRCM is documented in

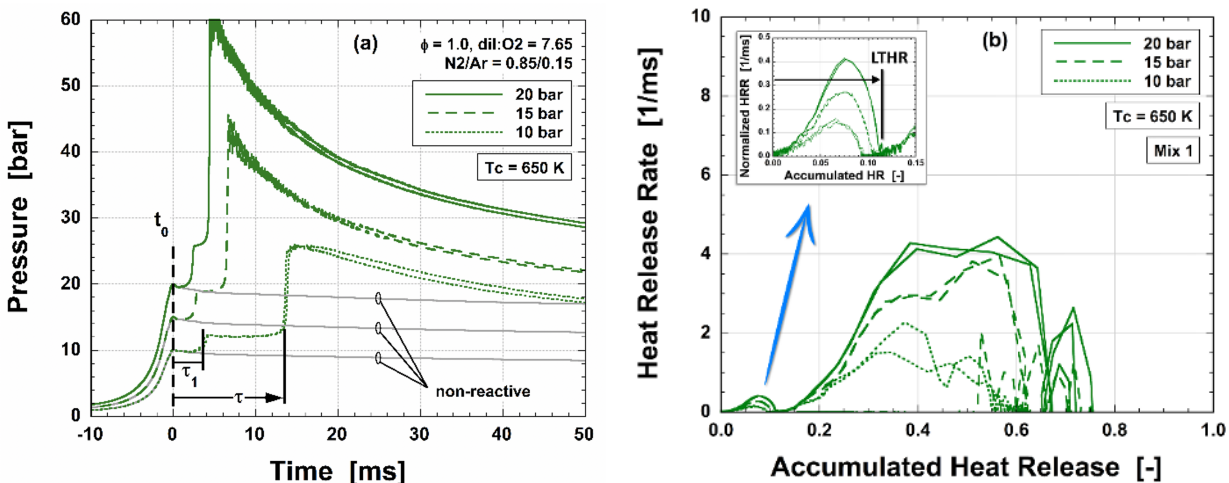


Figure 2: Representative (a) pressure and (b) normalized heat release profiles measured in the RCM for MPE/O₂/diluent mixtures at $T_C = 650$ K, $p_C = 10, 15, 20$ bar. Grey lines in (a) are corresponding non-reactive pressures used to identify the end of compression, facilitate heat release rate calculations and derive volume histories for chemical kinetic modeling.

Fridlyand et al. 2019, leading to 1.0% in conservative estimate to T_C [24]. Heat release rates (HRRs) and integrated, or accumulated heat release (aHR) are calculated as described in Goldsborough et al. 2019, where again, the non-reactive measurements are used to estimate conductive and enthalpic losses to the reaction chamber walls and piston crevices, respectively [28]. Figure 1b illustrates representative heat release behavior where the normalized HRRs are plotted as functions of aHR. These parameters are normalized by the lower heating values of the mixtures. The inset highlights the first-stage, or low-temperature heat release process (LTHR), where the inflections in the curves near $aHR = 0.10$ are taken to indicate the end of LTHR, as highlighted for the $p_C = 20$ bar condition. As with Fig. 1a, excellent shot-to-shot consistency is evident in the calculated rates of heat release. Goldsborough, et al. 2019 discussed limitations of the current approach towards mis-accounting for preliminary exothermicity, and challenges in comparing against model results [28]. The methodology is able to extract and account for (within uncertainties) heat release that occurs toward the end of the compression stroke, as observed in the current dataset.

We modeled these experiments two different ways. First we used the conventional zero-order approach, modeling the system as an adiabatic constant volume reactor having the

Author Manuscript

initial mixture composition and temperature T_C computed using Eq. 2 starting at the compression time, t_0 . Secondly, we used a more sophisticated parameterized reactor model, starting at $t = 0$ to include chemistry occurring during the compression stroke, and using the actual $V(t)$ of the apparatus and the time-dependent enthalpy and conductive heat losses inferred from the matching non-reactive traces using the method of Goldsborough. In this case we are modeling the ‘adiabatic core’ of the gas, since that zone usually ignites before the cooler gas near the cylinder walls. As shown later in Figure 13, these two different approaches to modeling the RCM experiments give quite different predictions for ignition times.

2.5 Model Construction

A detailed chemical reaction mechanism for methyl propyl ether oxidation was constructed using the Reaction Mechanism Generator (RMG) software for flux-based automatic mechanism generation [29]. RMG has been used to successfully generate models in many similar contexts [30–34]. Within RMG reactions are divided between the core and edge. Core reactions are reactions involving (core) species that RMG has decided are important enough to include in the mechanism. Edge reactions are reactions that RMG has generated from reacting core species together to produce new (edge) species that may be important to include. Each iteration reaction fluxes to edge species are calculated over the course of a set of simulations and if the flux to a species becomes sufficiently high relative to a characteristic flux that species is moved from the edge to the core.

The RMG mechanism was seeded with the reactions and thermochemistry from Burke et al. 2012 and Hashemi et al. 2016 [35, 36]. Additional thermochemical data was drawn from the RMG libraries: primaryThermoLibrary, thermo_DFT_CCSDTF12_BAC, CBS_QB3_1dHR and DFT_QCI_thermo that are mostly experimental or from high level calculations. All thermochemical parameters not included in those libraries or calculated in this study were drawn from RMG’s Benson style thermochemical group additivity method

[29, 37]. All rates not included in those libraries or calculated in this study were drawn from RMG’s rate rules and training reaction database [29].

The model refinement process is illustrated in Figure 3. Each iteration an RMG model was generated for the conditions of interest using the chemical knowledge in RMG’s database and calculations from this study. This model was compared against experimental data and then sensitivities to all rate coefficients and Gibbs energies of formation were calculated for key and observable species concentrations to determine what species thermochemistry and rate coefficients were sensitive. Sensitive thermochemistries and rate coefficients were then calculated quantum mechanically or estimated using literature for use in the next iteration. During refinement the model was generated for stoichiometric combustion of methyl propyl ether with air at 400–1650 K and 0.3–100 bar. RMG automatically identifies chemically-activated reaction pathways, and estimates the pressure-dependence of rate coefficients [38]. In the case of barrierless reactions which can’t be computed using conventional transition state theory, literature values and analogies were used [39–42]. The final RMG model generation run for this study was run out to 443 species on the MPether_do_not_delete branch of RMG-Py and the MPether_do_not_delete branch of RMG-database available from the ReactionMechanismGenerator Github organization.

The reactions of the resulting mechanism were analyzed for collision limit violations greater than a factor of 2.5 in the 600–1500 K and 1–100 bar range. Violators from literature reactions included in the seed mechanisms are listed in Table 1.

Table 1: Collision limit violating reactions from the seed mechanisms.

Number	Reaction
1	$\text{H}_2 + \cdot\text{CH} \rightarrow \cdot\text{CH}_3$
2	$\text{H}\cdot + \text{:CH}_2 \rightarrow \cdot\text{CH}_3$
3	$\text{C}\cdot + \text{CO} \rightarrow \cdot\text{C}\begin{array}{l} \diagup \\ \diagdown \end{array}\text{O}\cdot$
4	$\text{H}\cdot + \cdot\text{CH} \rightarrow \text{:CH}_2$
5	$\text{H}\cdot + \text{HC}\equiv\text{C}\cdot \rightarrow \text{HC}\equiv\text{CH}$

Of these Reactions 1 and 2 were derived from fits to data far out of the temperature range

of interest in this study and were removed from the mechanism. Reaction 3 only violates the collision limit near 100 bar, outside the range of the experiments in this study. Since this is likely just a consequence of being fitted (in the reverse direction) to a third body form that assumes a low pressure limit it was left in the mechanism. Reactions 4 and 5 were refit reducing the reverse rate coefficient values to prevent collision limit violations in the forward direction at each temperature. The simulations were not noticeably affected by the refitting and were not sensitive to any of the violators. Additionally a number of rate coefficients were improved after generation. Reactions relevant to this discussion are listed in Table 2. The rate for Reaction 6 from Hashemi et al. 2016 is referenced to Lu et al. 2010,

Table 2: Reactions related to modifications after mechanism generation.

Number	Reaction
6	$\text{:CH}_2 + \text{H}_2 \rightarrow \text{H}\cdot + \cdot\text{CH}_3$
7	
8	
9	
10	
11	
12	
13	
14	
15	
16	

but differs slightly from that reference and so was replaced with the exact value from Lu et al. 2010. The rate for Reaction 7 was replaced with an analogy to the rate calculated in this study for Reaction 8 [43]. The rates for Reaction 9 and the sequence formed by Reactions 10 and 11 were replaced with our quantum chemistry calculations: $A=7.87e4 \text{ s}^{-1}$, $n=1.72$, $E_a=59.4 \text{ kJ/mol}$ and $A=114 \text{ s}^{-1}$, $n=2.69$, $E_a=28.2 \text{ kJ/mol}$ respectively. Reaction 12 from Hashemi et al. 2016 is an analogy to an experimental measurement of the rate at which the reactants react with an assumed product [44]. However, this channel has been recently shown to primarily proceed to a different set of products shown in Reaction 13 [45]. We have

therefore changed the products of Reaction 12 to those of Reaction 13 in the mechanism. The four hydrogen abstraction reactions between $\text{CH}_3\text{CH}_2\text{OO}$ and MPE were reversed and re-estimated using RMG's rate rules in the direction with $\text{CH}_3\text{CH}_2\text{OO}$ and MPE as the reactants to improve branching accuracy. The pressure dependent network containing Reactions 14–16 as path reactions was regenerated using Arkane's pressure dependent network explorer tool integrating quantum chemistry calculations for Reactions 14–16: $A=1.70\text{e}8 \text{ s}^{-1}$, $n=1.51$, $E_a=31.6 \text{ kJ/mol}$, $A=3.37\text{e}11 \text{ s}^{-1}$, $n=0.569$, $E_a=20.0 \text{ kJ/mol}$ and $A=1.33\text{e}12 \text{ s}^{-1}$, $n=0.406$, $E_a=79.4 \text{ kJ/mol}$ respectively.

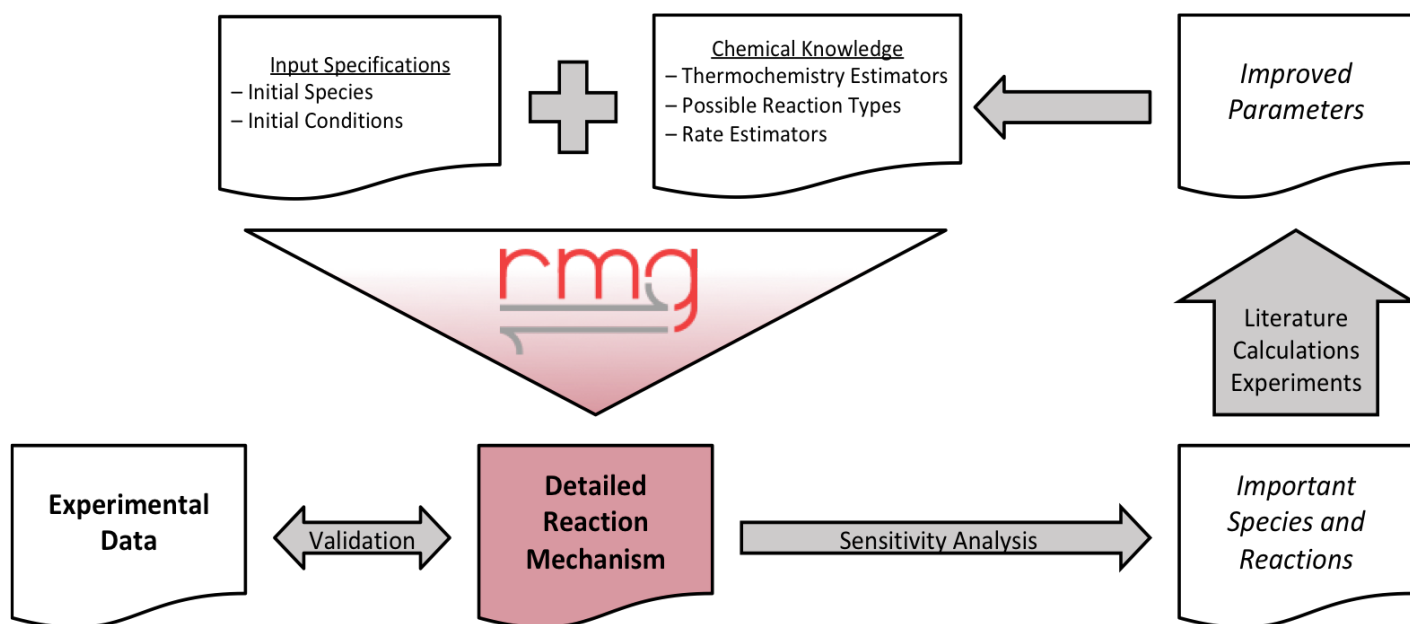
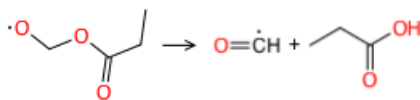


Figure 3: RMG model construction workflow

2.6 Rate Constant Comparisons

As a part of this study 91 rate coefficients were calculated and 138 sets of thermochemical parameters were computed using quantum chemistry. The results of these calculations are presented in the supplementary information. Most of the 91 computed reactions were qualitatively unsurprising. However, we did discover one unexpected reaction that turns out to be quite important:



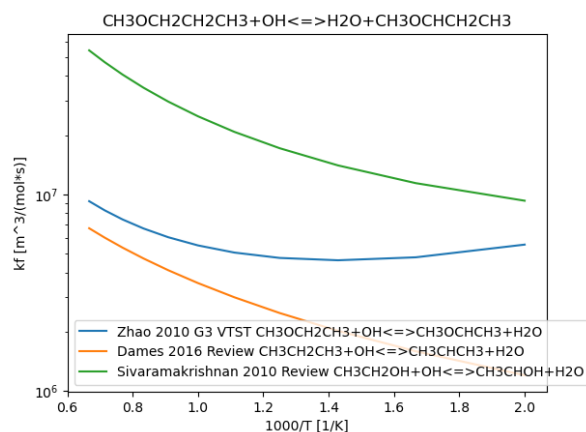
While we had expected the reactant to undergo a normal beta-scission reaction forming CH_2O and $\text{C}_3\text{H}_5\text{O}_2$, calculations indicated a concerted H-shift as the C–O bond breaks. Our computed high-pressure-limit rate parameters for this reaction are $A = 7.44e11 \text{ s}^{-1}$, $n = 0.444$, $E_a = 9.64 \frac{\text{kcal}}{\text{mol}}$.

Literature reviews were done on the most important rate coefficients; a few are shown here in Figure 4. Figure 4a examines hydrogen abstraction by OH from the central carbon of MPE. This reaction goes through a floppy transition state which prevents it from being calculated using traditional transition state theory. The rate parameters for the reaction from Zhao 2010 are used in this paper because it is most similar to the reaction of interest. It agrees quite well with the predictions in Dames 2016 and Sivarmakrishnan 2010 for similar reactions.

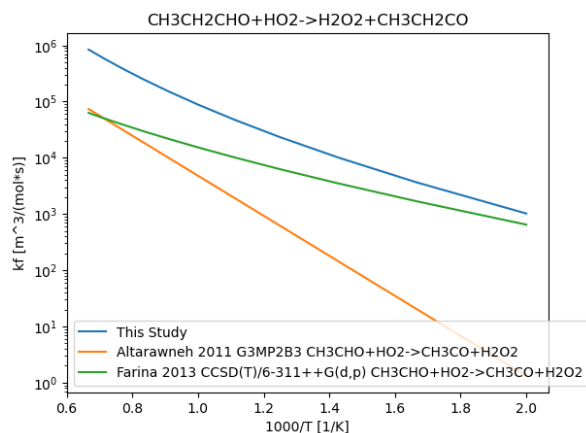
Figure 4b shows a comparison of rates similar to hydrogen abstraction by HO_2 from the carbonyl hydrogen of propanal. The rate coefficients for the two carbon analogue to this reaction are noticeably smaller than the values calculated for the actual reaction in this study [46, 47]. However, the latest study Farina 2013 only differs by about a factor of four at $T=1000 \text{ K}$ and the differences between the Farina 2013 and Altarawneh 2011 rate coefficients over the range of interest is roughly as large as the difference between Farina 2013 and the calculation for the actual reaction.

Figure 4c shows a comparison of rates similar to the 1,2-ROR elimination of MPE. The rate calculated in this study agrees very well with the rate from Yasunaga 2008 for ethyl tert-butyl ether [48]. Agreement with the more analogous reaction from Sumathi 2003, is not quite as good, but still within a factor of four at high temperatures.

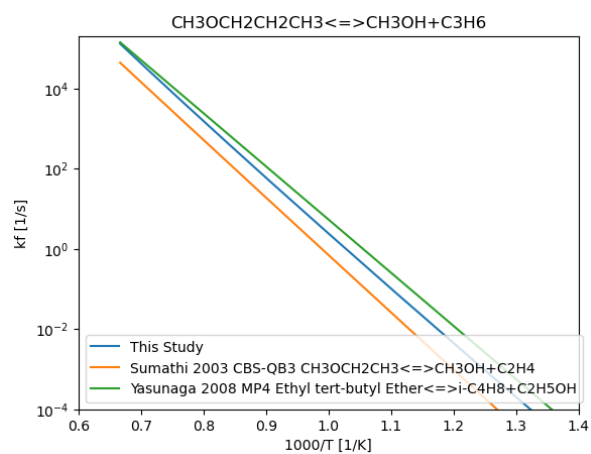
Figure 4d shows a comparison of rates for beta-scission of the $\text{CH}_3\text{OCHCH}_2\text{CH}_3$ radical. The dimethyl ether analogues to this reaction are about a factor of three faster at high temperatures than the values calculated in this study.



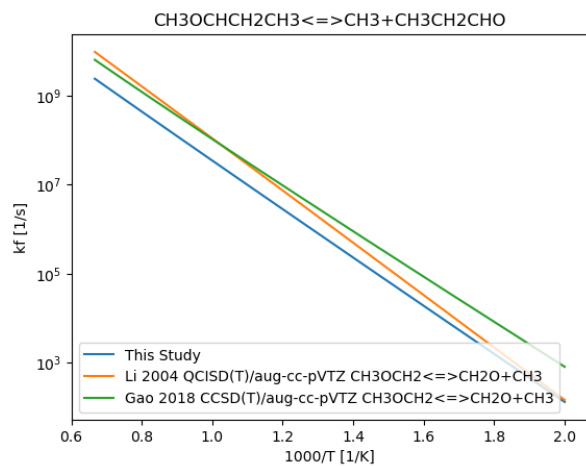
(a) We use Zhou et al.'s value for this reaction.



(b) We computed this rate using the G4 method.



(c) Figure shows high pressure limit coefficients. The kinetic model includes RMG-estimates of the corrections for fall-off and chemical-activation.



(d) Figure shows high pressure limit coefficients. The kinetic model includes RMG-estimates of the corrections for fall-off and chemical-activation.

Figure 4: Comparisons with literature for key rate coefficients. The estimated reaction is listed in the title of each plot.

3 Results and Discussion

3.1 Shock Tube

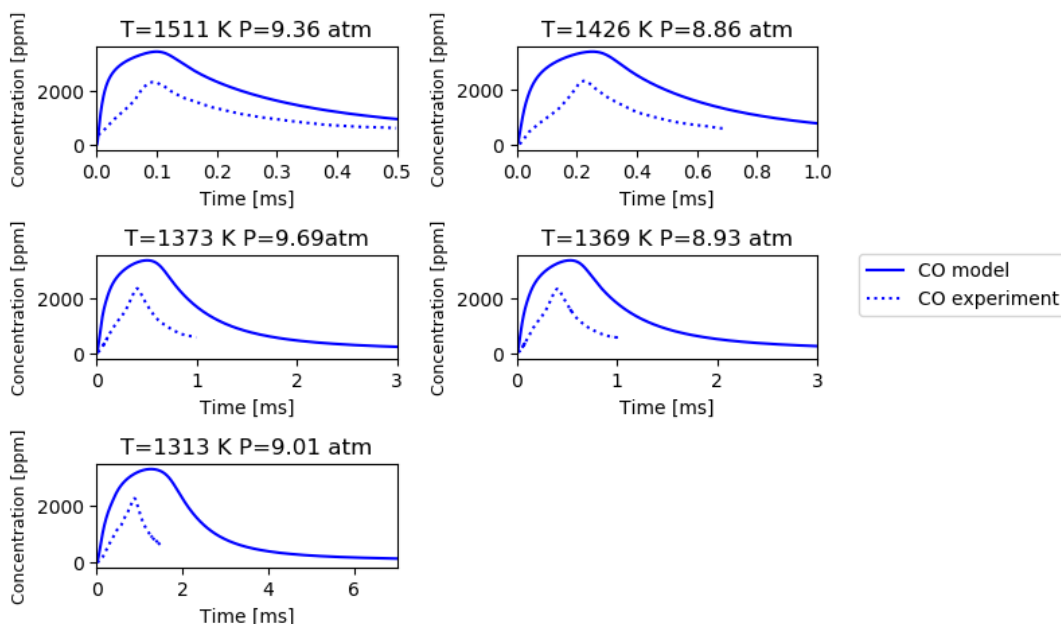


Figure 5: Shock tube oxidation of MPE

The experimental shock tube measurements under oxidative conditions, and the corresponding model predictions are shown in Figure 5. The measurements and predictions agree reasonably well. CO peak times agree within a factor of 1.5 for all experiments. Predicted peak heights are within about 34% of experiment.

A similar comparison for data measured at pyrolysis conditions is presented in Figure 6. The model very closely emulates the experimental data, generally within the uncertainties of the experiment and the model. Because the model agreed so well with these experimental data even for the first version of the model tested, we did not make any refinements to the model to improve agreement with this data.

At these high temperatures, particularly in the pyrolysis case, the various competing unimolecular reactions of MPE are very important, and strongly affect the formation of CO and other products. These reactions are listed in Table 3 and their rate coefficients are plotted

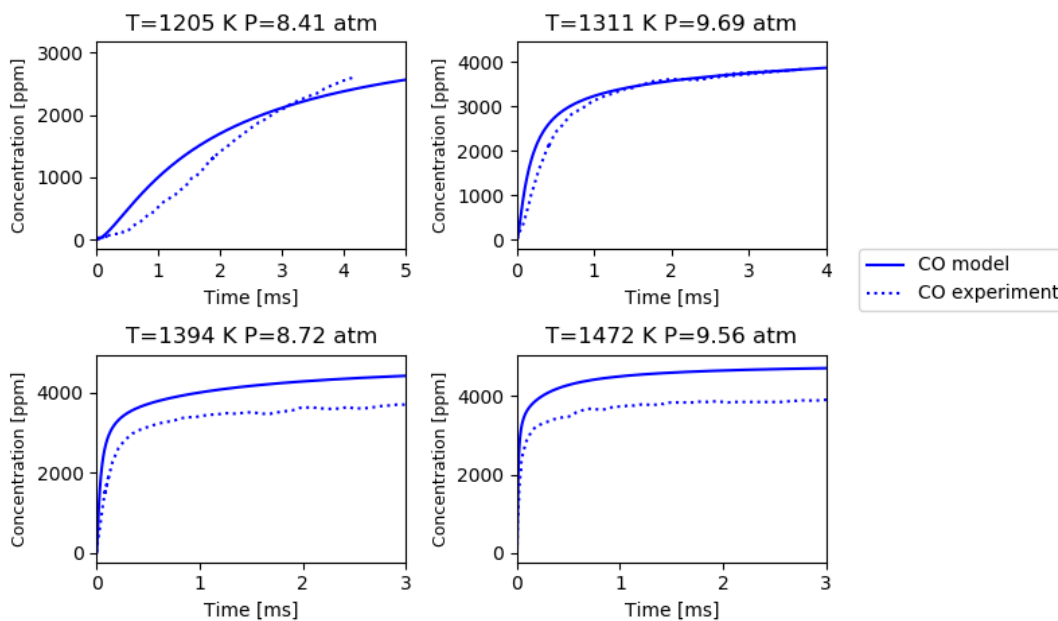


Figure 6: Shock tube pyrolysis of MPE

in Figure 7. At lower temperatures Reaction 18 dominates, while above 1300 K Reaction

Table 3: Dominant MPE unimolecular reactions.

Number	Reaction
17	<chem>CCOC >> [O]C + C[CH2]</chem>
18	<chem>CCOC >> CO + C=C</chem>
19	<chem>CCOC >> CO + C[CH2]</chem>
20	<chem>CCOC >> C[CH2] + CO</chem>

17 dominates. Except for Reaction 18, which was computed using quantum chemistry in this study (see Figure 4c), all of these reactions are barrierless in the bimolecular direction, making them difficult to compute accurately and thus were estimated using RMG. While the rate coefficients for radical recombination reactions only span about an order of magnitude making them easy to estimate within about a factor of 2 or 3 there is additional inherent uncertainty due to approximations made in RMG’s pressure dependent rate coefficient calculations of about a factor of 2 or 3 [38]. Together with uncertainties in the thermochemistry, this gives about a factor of 5 uncertainty in the absolute MPE decay rate, and also significant uncertainties in the branching ratio between these different decomposition channels. These

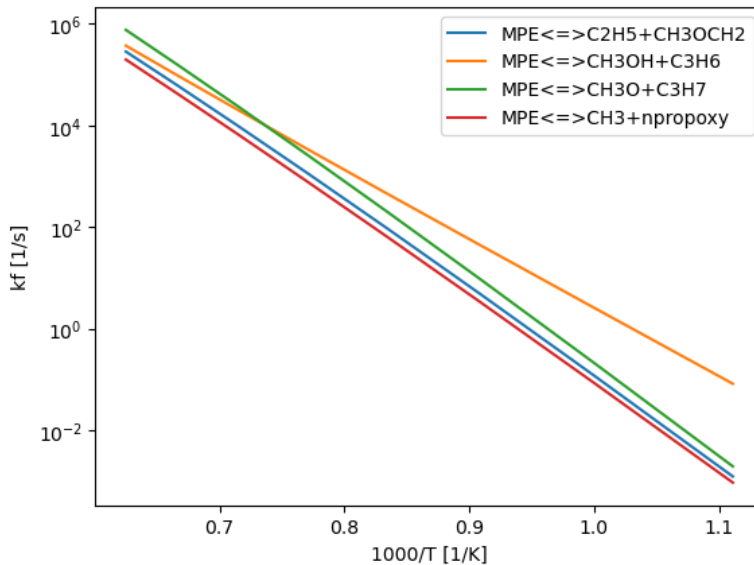


Figure 7: Dominant MPE unimolecular reactions at 10 bar.

uncertainties are more than enough to explain the observed deviations between model and experiment in Fig. 5, indeed it seems that the level of agreement between the model and the shock tube data is better than we are entitled to expect considering all the uncertainties.

3.2 Flow Tube

Comparisons between the flow tube experiments and simulations for 2 s residence times are available in Figures 8 and 9. Broadly the model predicts an earlier transition from the low to high conversion regime at 2 s than is observed experimentally. Focusing on temperatures where model and experiment agree better on conversion, methane, propene, ethene and propanal agree with the experiments and the comparison with CO and CO₂ makes sense. The yields of acrolein and ethane are predicted satisfactorily at 825–850 K, but these minor products are underpredicted by more than an order of magnitude at $T < 750$ K and at 900 K. Both the data and the model show strong and somewhat peculiar temperature dependence in this temperature range.

A comparison with 5 s residence time data is shown in Figures 10 and 11. At 5 s the measured MPE conversions and the model predictions agree better, both showing significant

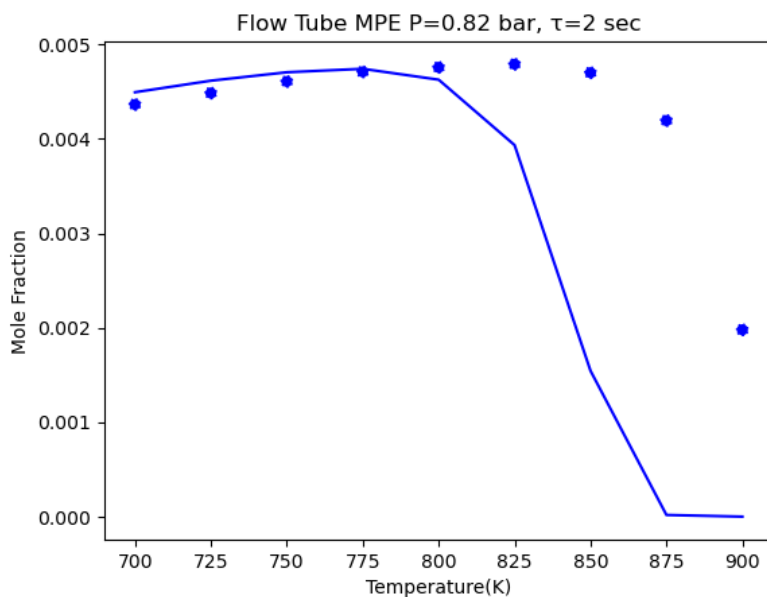


Figure 8: Predicted and measured mole fraction of MPE exiting the flow reactor at the high flow rate (2 sec residence time).

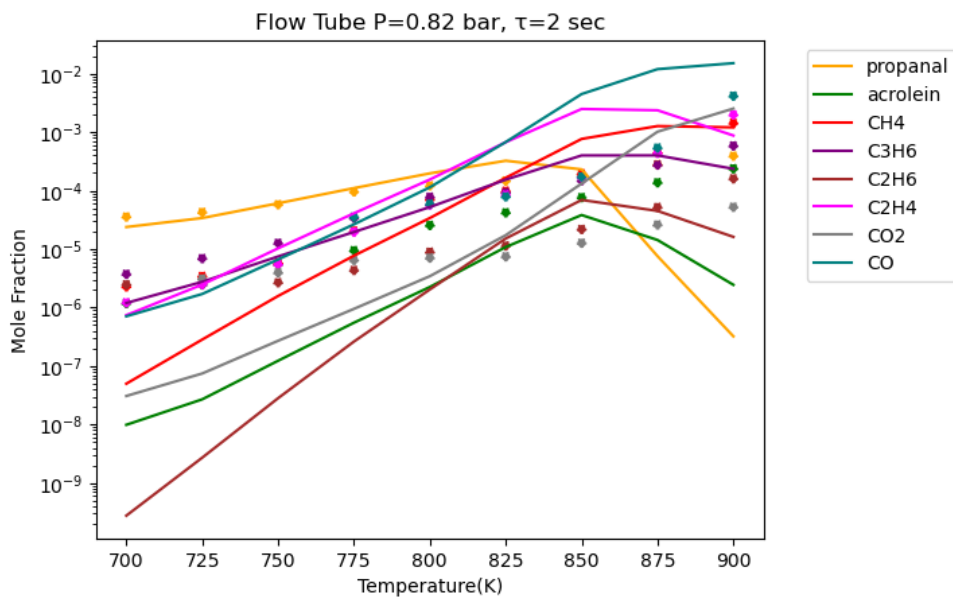


Figure 9: Flow tube product comparison at a 2 second residence time.

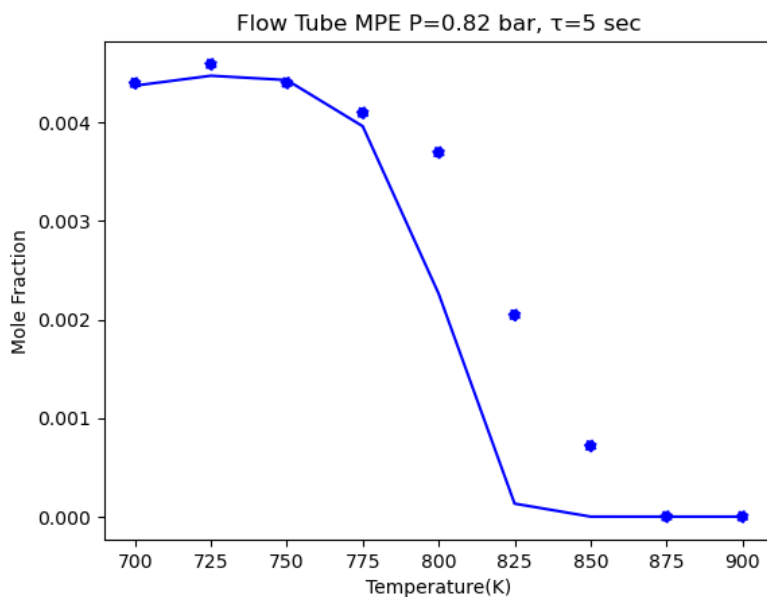


Figure 10: Predicted and measured mole fraction of MPE exiting the flow reactor at the low flow rate (5 s residence time).

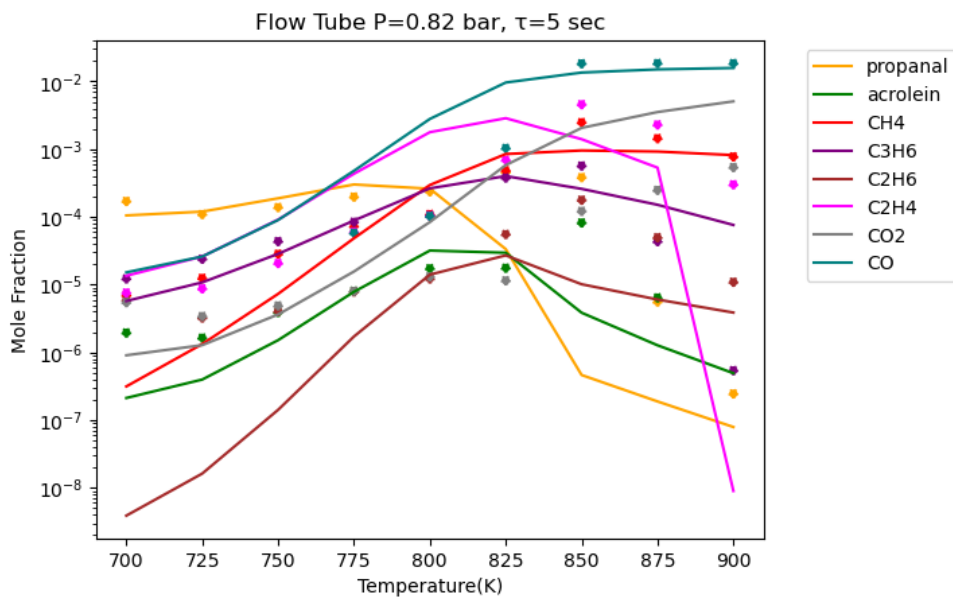


Figure 11: Flow tube product comparison at a 5 s residence time.

changes in conversion at about the same temperatures (within 25 K). Methane, ethene, acrolein and propene yields agree quite well except at lower temperatures, where the model slightly overpredicts the reactivity. The model predicts the CO yields quite well. Propanal matches very well at low temperatures, but the model shows the drop-off in propanal yield about 50 K lower than where it is found in the experiments. Ethane yield is under-predicted at most temperatures, and CO₂ yield is overpredicted at high temperatures.

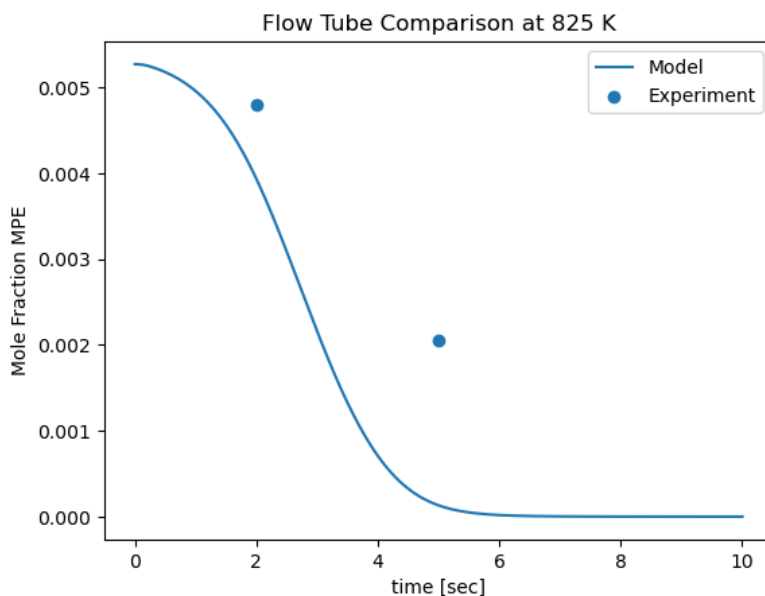
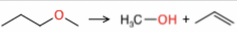
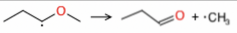
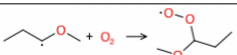
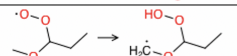
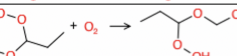
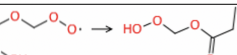
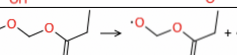
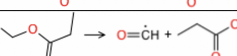
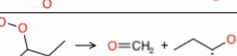
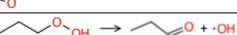
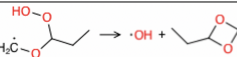
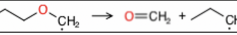
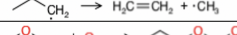
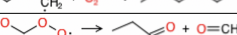
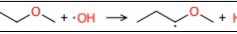



Figure 12: Predicted MPE exit mole fraction as a function of residence time in the flow reactor, with measured data for 2 sec and 5 sec.

Much of the disagreement between model and experiment derives from differences in MPE conversion. So it's worth having a detailed discussion of the chemistry driving MPE conversion. At higher temperatures (e.g. in the shock tube experiments) MPE can simply pyrolyze to stable products through Reaction 18. However, at the lower temperatures of the flow tube experiments MPE is primarily consumed by hydrogen abstractions to form MPE radicals. For the dominant MPE radical there is competition between Reaction 21 and Reaction 22, pyrolysis and addition to O₂ respectively. Reaction 22 is significantly reversible at high T and low O₂ partial pressure, but Reactions 23-25, 10, and 28 carry the oxidation chemistry forward.

Table 4: Key flow tube reactions.

Number	Reaction
18	
21	
22	
23	
24	
25	
26	
27	
10	
11	
28	
8	
29	
30	
31	
32	

However, at the partial pressure of O_2 used in the flowtube, Reaction 21 only becomes fully competitive with Reaction 22 at 900 K. After the first addition to O_2 and Reaction 23 there is competition between a second addition to O_2 (Reaction 24) leading to formation of additional radicals through Reactions 24-27, beta-scission of the radical through Reactions 10 and 11 and cyclization through Reaction 28. According to the model, Reactions 24-27 and 28 dominate below 600 K and Reactions 10 and 11 tend to dominate above 600 K. It's worth noting that Reaction 27 involves a concerted H shift that was unexpected by us, and so would not have been discovered by RMG. This emphasizes the importance of quantum chemical insight in the refinement of chemical mechanisms in general.

The second most dominant radical has two primary pathways, pyrolysis shown in Reaction 8 and addition to O_2 followed by pyrolysis shown in Reactions 30 and 31 the first path (Reaction 8) starts to dominate around 800 K.

Notice in Figures 8 and 10 the amount of MPE surviving through the reactor is a non-monotonic function of the temperature. At the lowest temperatures studied, the sequential addition of two O_2 's (reactions 22-23-24) is the key to making the radicals that consume MPE. However, each of these reactions is reversible, and as a consequence as the temperature increases above 700 K it becomes less and less effective at generating radicals – and so more of the MPE passes through the reactor unscathed. However, at higher temperatures a different method of creating radicals, $H_2O_2 \rightarrow 2 OH$ takes over. The H_2O_2 sequence has a more normal T-dependence, increasing MPE consumption as T increases.

Figure 12 compares simulated MPE mole fractions with the 825 K experiments. At these temperatures we expect MPE to be primarily consumed by hydrogen abstraction. In a simplistic analysis the half-life of MPE in the experiment is roughly 4.5 seconds while the model half-life is about 2.5 seconds which suggests the MPE consumption rate in the model is off by about a factor of 2 at 825 K.

Near these conditions, apart from the small molecule chemistry, MPE is by far most sensitive to Reaction 32, which has a very high sensitivity. At five seconds $\frac{dLn(w_{MPE})}{dLn(k)} \approx -5.5$.

This extreme sensitivity occurs because this reaction controls branching between the two MPE radicals. At this temperature the dominant radical $CO[CH]CC$ is still able to add O_2 and produce OH and other radicals, while the second most dominant radical cannot (it just decomposes). This makes the system uniquely sensitive to the OH abstraction rate forming this key radical (which is competing with all other pathways consuming OH).

For this sensitive reaction we have used analogy to the variational transition state theory (VTST) rate coefficients for the same sites on methyl-ethyl ether computed by Zhou et al. 2010 [39]. While this should be a good estimate, even assuming only 50% error in the rate coefficient a linear extrapolation of the sensitivity gives a resulting error of about a factor of 10 in the MPE mass fraction. Assuming a more realistic factor of 2 uncertainty in the rate coefficient gives a factor of about 45 uncertainty. Achieving better than the present factor-of-two accuracy predictions of the MPE consumption rate at these conditions would require knowing k_{30} at 825 K to an accuracy of 20%; this might be possible with a well-designed experiment but is certainly not easy and is beyond the scope of this present work. However, this made it impractical to achieve the accuracy necessary to improve the MPE conversion predictions in this study.

3.3 Rapid Compression Machine

Table 5: molar composition, compressed temperature range and compression ratio employed for each fuel/ O_2 /diluent mixture used in the RCM tests.

Mix	MPE	O_2	N_2	Ar	T_c [K]	CR
1	0.0189	0.1138	0.7368	0.1305	605–695	6.4
2	0.0189	0.1137	0.8674	0.0	705–818	12.1
3	0.0188	0.1131	0.4308	0.4373	820–942	12.1

A wide range of temperatures is covered in the RCM tests with $T_c = 600$ – 945 K, at compressed pressures of $p_C = 10, 15, 20$ bar using diluted, stoichiometric mixtures. Alterations to the compression ratio, diluent composition and initial temperature are used to

sweep from low to high temperature, as indicated by Table 5. The lowest temperatures facilitate evaluation of trends in τ_1 and LTHR, as these occur before the end of compression when $T_C > 700\text{K}$. The fuel is very reactive with short ignition delays; low pressure and low temperature are required to observe first-stage ignition. Figures 13 and 14 present summaries of τ_1 , τ , and LTHR, plotted as functions of inverse temperature. Excellent shot-to-shot consistency was observed across the entire span of experimental conditions. In Fig. 13 it can be seen that at the experimental conditions, the MPE/ O_2 /diluent mixtures exhibit low-, negative temperature coefficient (NTC), and intermediate-temperature behavior, where the measurement results are noticeably influenced by the test compression ratio and diluent composition. There appears to be little influence of pressure on τ_1 , while τ is significantly influenced by pressure at intermediate temperatures. In Fig. 14 it can be seen that the LTHR changes fairly monotonically across the temperature range, with trends found that are similar to those measured with gasoline-type fuels, i.e., higher pressures lead to greater LTHR while higher temperatures lead to decreased LTHR. The LTHR for PRF90/ O_2 /diluent mixtures measured in the ANL tpRCM at similar conditions are documented to be significantly less than MPE.

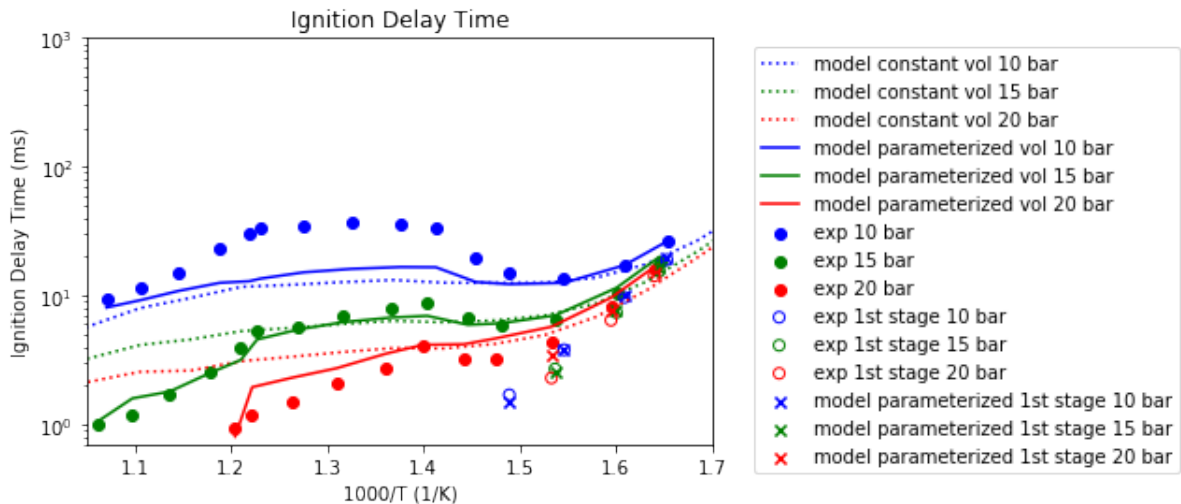


Figure 13: Measured vs. model-predicted ignition delays τ and end-of-first stage times τ_1 . Parameterized models account for heat losses and so changes in the adiabatic core volume using the measured $P(t)$ for non-reactive mixtures.

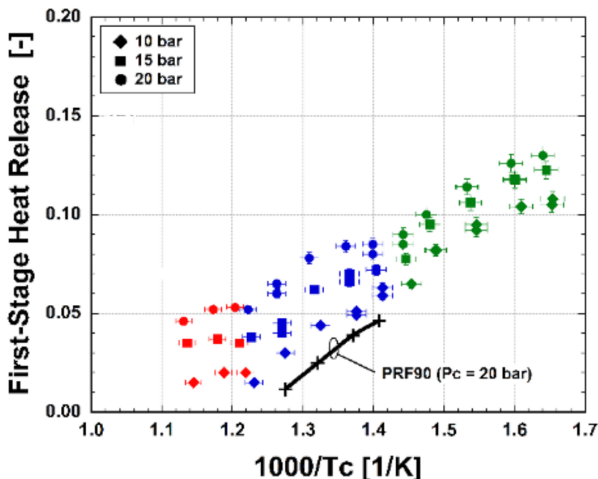


Figure 14: first-stage heat release presented as functions of inverse temperature for MPE $p_C = 10, 15$ and 20 bar. Color is used to indicate changes to compression ratio and/or diluent composition; green = Mix 1, blue = Mix 2, red = Mix 3.

Sometimes RCM experiments can be accurately predicted simply by simulating the contents of the reactor from the end of compression to ignition adiabatically at constant volume. However, as can be seen in Figure 15 for MPE the difference in compressed pressure between the unreactive and the reactive and simulated pressure traces at this condition is quite significant implying that there is significant reactive heat release during compression. For this reason we focus on parameterized volume simulations that use the RCM volume histories and account for heat losses. A comparison between RCM experiments and simulations is available in Figure 13. Both the parameterized and constant volume results are provided for comparison. The agreement with the parameterized runs is quite good within about a factor of 2, well within the uncertainties of the model parameters. The large difference in ignition delay between the 10 bar data and the 15 and 20 bar data is atypical of similar sized molecules so it's worth investigating differences in the simulations. We have identified two primary differences in the chemical pathways. The first lies in the two dominant low temperature feedback loops represented by the first ten reactions in Table 6 these OH feedback loops control radical production in the low temperature regime. While the rate coefficients k for the reactions in Table 6 are only weakly pressure-dependent at the important RCM

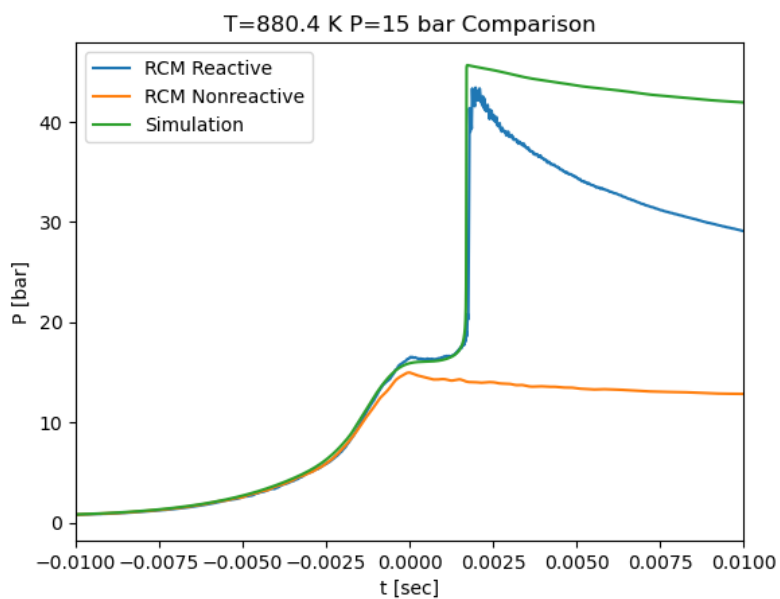


Figure 15: Comparison between experimental reactive and nonreactive pressure traces and simulated pressure using the RCM volume history.

Table 6: Key low temperature RCM reactions.

Number	Reaction
22	
23	
24	
25	
26	
30	
33	
34	
35	
36	
10	
11	
37	
38	

conditions, the overall process is pressure-dependent, since there are bimolecular reactions (e.g. additions to O_2) competing with unimolecular reactions. Since the addition to O_2 path generates more radicals, radical production will be greater at higher pressures. This difference in branching between the 10 bar and 15 bar cases can be seen at 600 K in Figures 16 and 17.

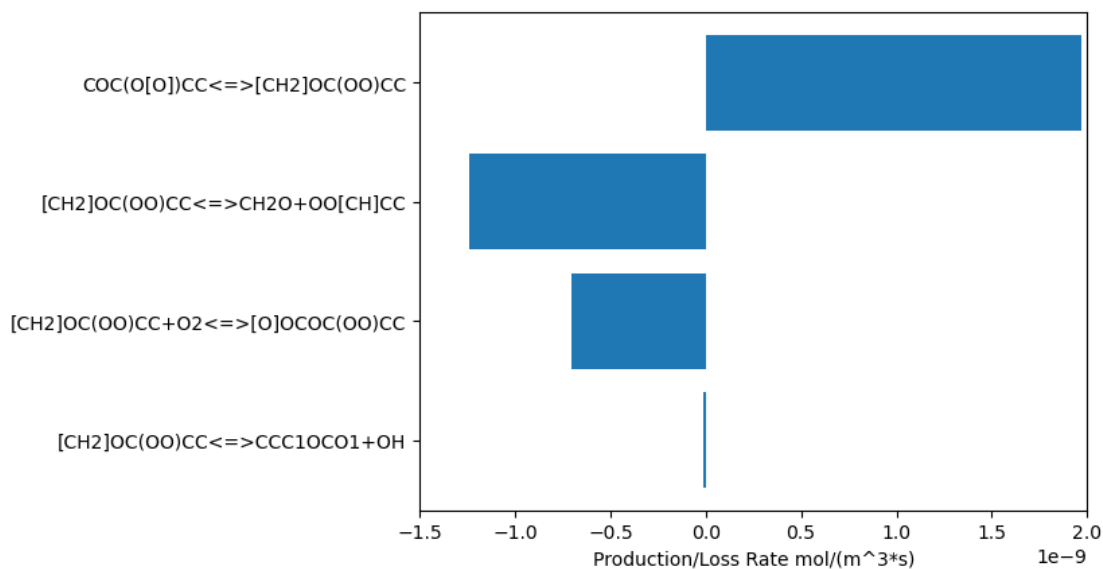


Figure 16: Computed reaction production/loss contributions for $[CH_2]OC(OO)CC$ when T reaches 600 K in the 10 bar / 873 K compressed temperature RCM experiment.

The second difference occurs later around 810 K in the simulation and can be seen clearly in Figures 18 and 19. The huge difference in the x-axis scales reflects the difference in total radical production rate at the two conditions. The dominant source of radicals at this point, Reaction 39, in the 15 bar simulation doesn't even show up on the plot for the 10 bar simulation. This reaction occurs as part of the sequence represented by Reactions 40-43, 39 and then 44-49. In net terms of radicals this pathway converts two HO_2 radicals into two much more reactive OH radicals. There's also an important side reaction represented by Reaction 50 that can leak flux from the pathway. It's easy to argue that Reaction 40 should run faster in the higher pressure simulations since it is bimolecular and we already expect the radical concentration to be higher due to the lower temperature chemistry. However, it turns out that additionally the loss pathways for CH_3CH_2OO are completely different at the

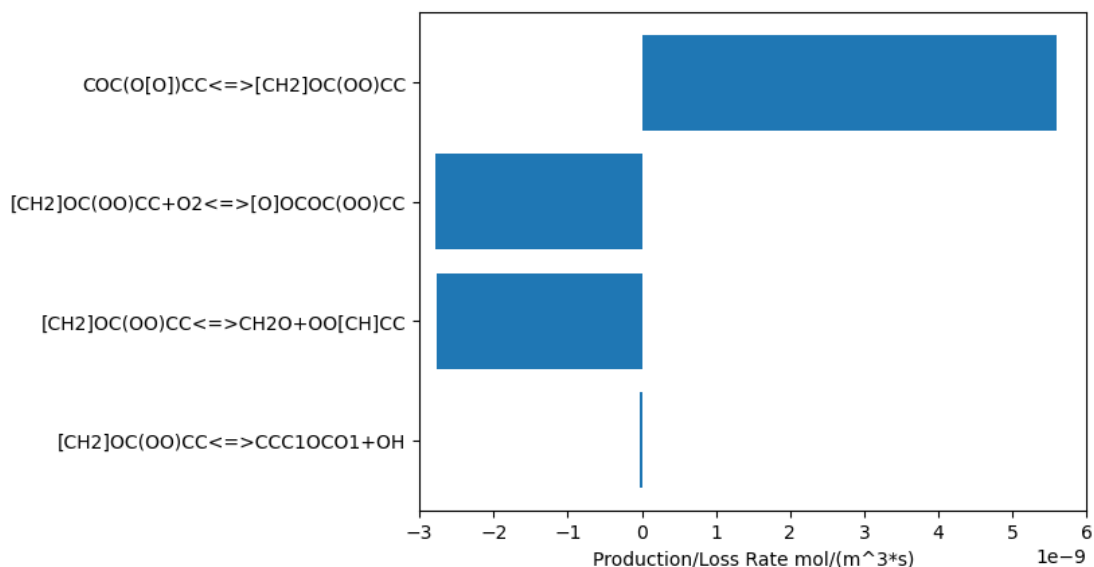


Figure 17: Computed reaction production/loss contributions for [CH2]OC(OO)CC when T reaches 600 K during compression in the 15 bar / 880 K compressed temperature RCM experiment.

Table 7: Reactions affecting radical generation from propanal decomposition.

Number	Reaction
39	<chem>CC(O)O >> CC(O)O >> CC(O)O + OH</chem>
40	<chem>CC=O + HO2 >> H2O2 + CC=O</chem>
41	<chem>CC=O >> H3C-CH2 + CO</chem>
42	<chem>H3C-CH2 + O2 >> CC(O)O</chem>
43	<chem>CC(O)O + HO2 >> CC(O)O + O2</chem>
44	<chem>CC(O)O >> O=CH2 + CH3</chem>
45	<chem>CH3 + O2 >> CC(O)O</chem>
46	<chem>CC(O)O + HO2 >> CC(O)O + O2</chem>
47	<chem>CC(O)O >> O-CH3 + OH</chem>
48	<chem>O-CH3 >> O=CH2 + H</chem>
49	<chem>H + O2 >> HO2</chem>
50	<chem>CC(O)O >> H2C=CH2 + HO2</chem>

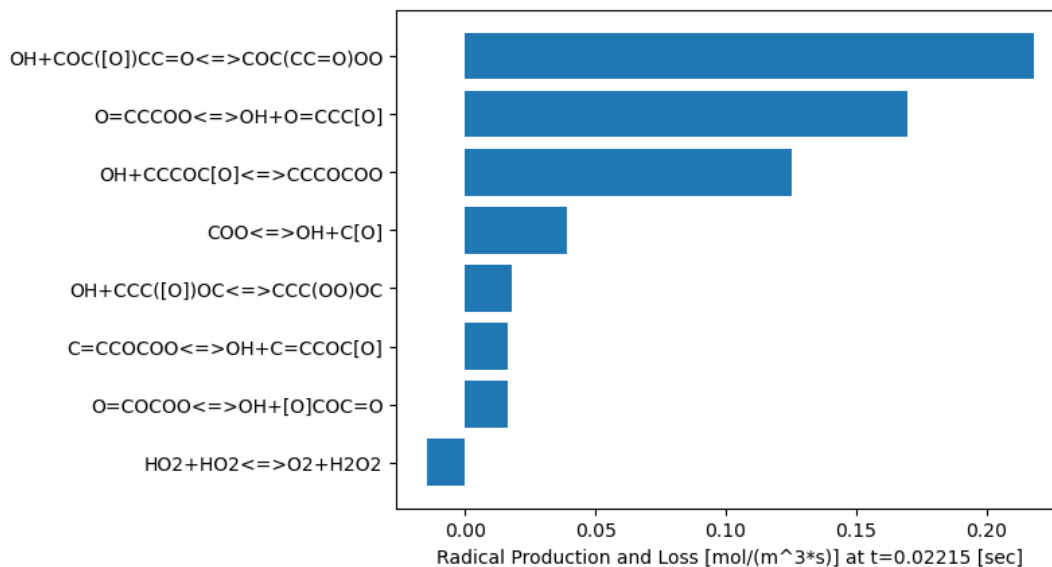


Figure 18: Computed reaction production/loss contributions for all radicals when T reaches 810 K during compression during the 10 bar / 873 K compressed temperature RCM experiment.

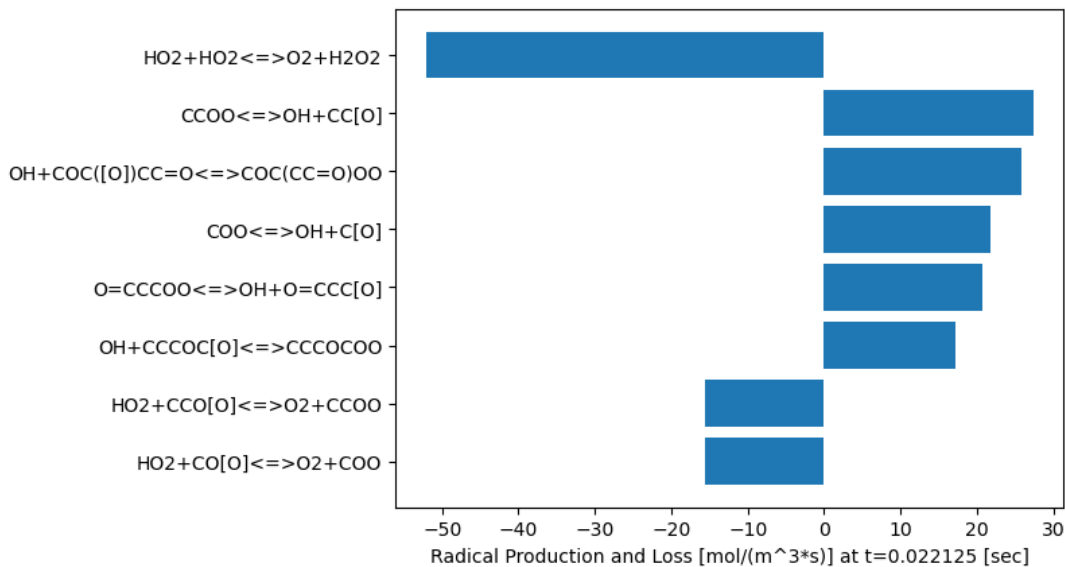


Figure 19: Computed reaction production/loss contributions for all radicals when T reaches 810 K during compression in the 15 bar/ 880 K compressed temperature RCM experiment.

two conditions. In Figures 20 and 21 it can be seen clearly that in the 10 bar simulation the pyrolysis reaction that leaks from the pathway dominates while in the 15 bar simulation the hydrogen abstraction pathway dominates. This is due to the fact that the HO_2 concentration is much higher in the 15 bar simulation.

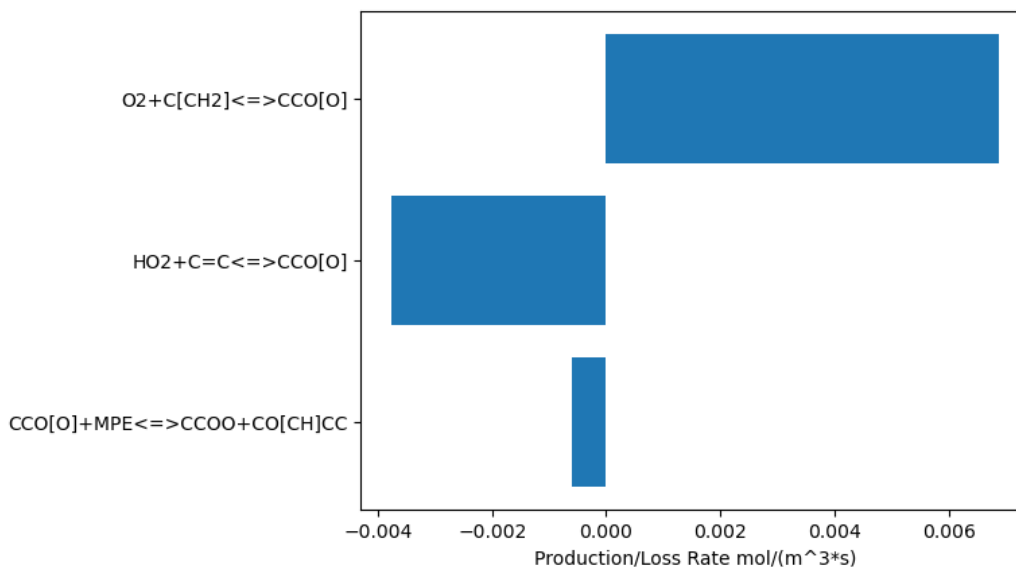


Figure 20: Computed reaction production/loss contributions for $\text{CH}_3\text{CH}_2\text{OO}$ at 810 K during compression in the 873 K and 10 bar compressed temperature simulation.

3.4 Compression Ignition Analysis

As discussed earlier, interest in ether fuels focuses on their use as diesel additives in a compression ignition engine. This makes it valuable to understand how MPE will behave under compression ignition conditions. This behavior is usually analyzed within an Ignition Quality Tester (IQT) or a Constant Volume Combustion Chamber (CVCC) run.

We modeled these conditions based heavily on prior work on the Two Stage Lagrangian model in literature [49–51]. In an IQT/CVCC a liquid jet of fuel is injected into a cylinder of heated air. As hot air is entrained by the jet the fuel vaporizes and ignites forming a flame at the edge of the jet. The Two Stage Lagrangian model models this process using two reactors: a core jet reactor and a steady state flame reactor where hot air flows in representing the

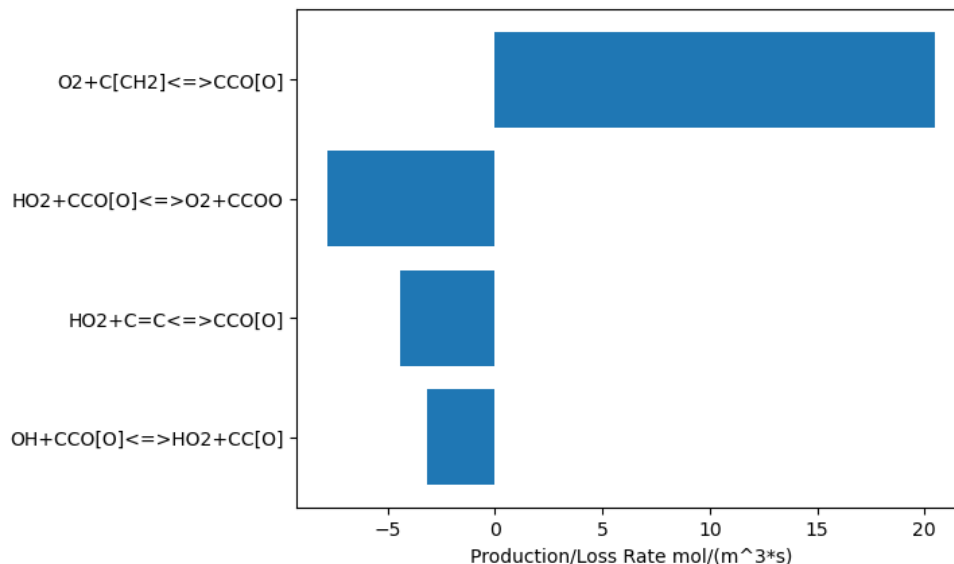


Figure 21: Computed reaction production/loss contributions for CH₃CH₂OO at 810 K during compression in the 880 K and 15 bar compressed temperature simulation.

interface between the cold core jet and the hot air. Please see Alfazazi et al. 2016 for a more detailed description of this model [49]. If one is not interested in the behavior of the post-ignition flame the flame reactor can be removed. This was done in Alfazazi et al. 2016 by fixing the flame reactor temperature to 350 K in order to turn off chemistry in the flame reactor.

In this study the IQT was modeled using a constant pressure semi-batch reactor in the ReactionMechanismSimulator software [52]. This approach differs from the approach in Alfazazi et al. 2016 only by removing the flame reactor and having air flow directly to the core reactor rather than fixing the temperature for the flame reactor to a low value. The same as prior studies the initial liquid nature of the fuel was handled by adjusting the initial temperature to preserve adiabatic flame temperature and by adjusting the inlet diameter to preserve mass flow rate [49–51]. For the model run we used a set of real IQT parameters and conditions from Alfazazi et al. 2016. The air in the reactor was held at 720.0 K and 21.3 bar, the injected liquid fuel temperature was set to 326 K and the injector was given a diameter of 0.722 mm, an injection pressure of 179.26 bar and an injection time of 2 ms.

Plots of O₂ mole fraction, temperature and MPE mole fraction are available in Figures

22, 23 and 24. We are able to see ignition occurs at about 0.115 ms, 762 K and an equivalence ratio of about 70. After ignition when the flame forms in the jet this simulation stops being an accurate representation of the real system.

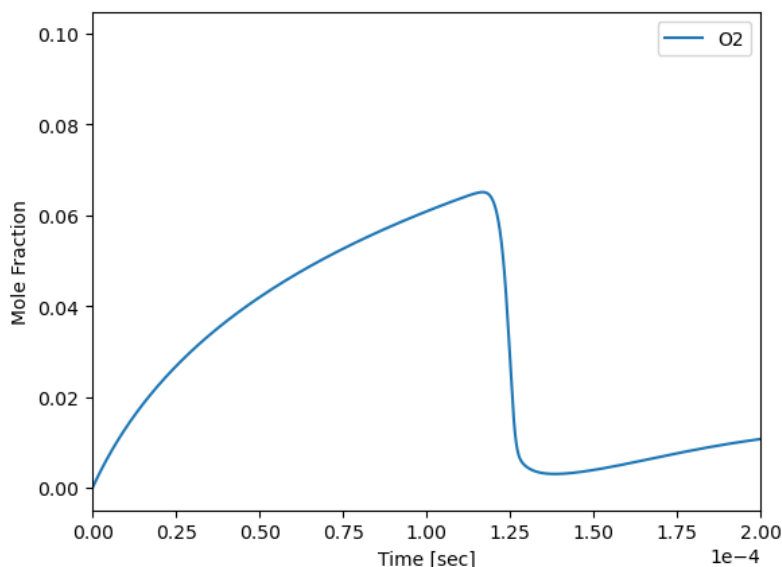


Figure 22: O₂ mole fraction in the IQT simulation.

Because the temperature is so low and the equivalence ratio is so high early in the simulation most chemistry doesn't start up until about 0.07 ms. A flux diagram and radical rate of production plot at this time point are available in Figures 25 and 26. The temperature at this time point is about 672 K. At this condition in the IQT, the MPE concentration is so high that the majority of the $CCC(O[O])OC$ bimolecularly abstracts a hydrogen from MPE to make a hydroperoxide $CCC(OO)OC$. At these conditions, the direct reaction of O₂ with MPE and the decomposition of $CCC(OO)OC$ both form more radicals than the conventional ketohydroperoxide feedback loop which dominates in more fuel-dilute conditions.

The same plots for 0.1 ms are available in Figures 27 and 28. At this time point the temperature is about 729 K. While the ketohydroperoxide feedback loop starting from $CC[CH]OC$ is running at this condition, beta-scission of the $[CH_2]OC(OO)CC$ radical dominates severely reducing its effectiveness. At this condition, decomposition of the ROOH formed at earlier times dominates radical production.

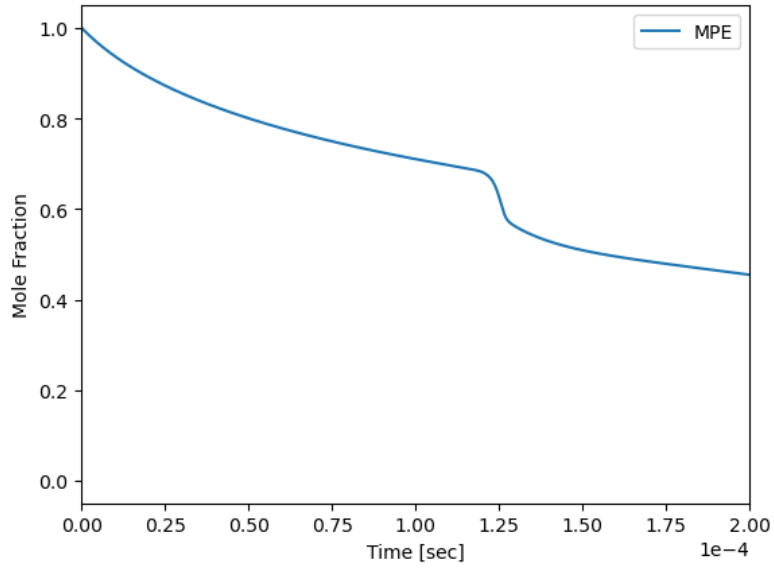


Figure 23: MPE mole fraction in the IQT simulation

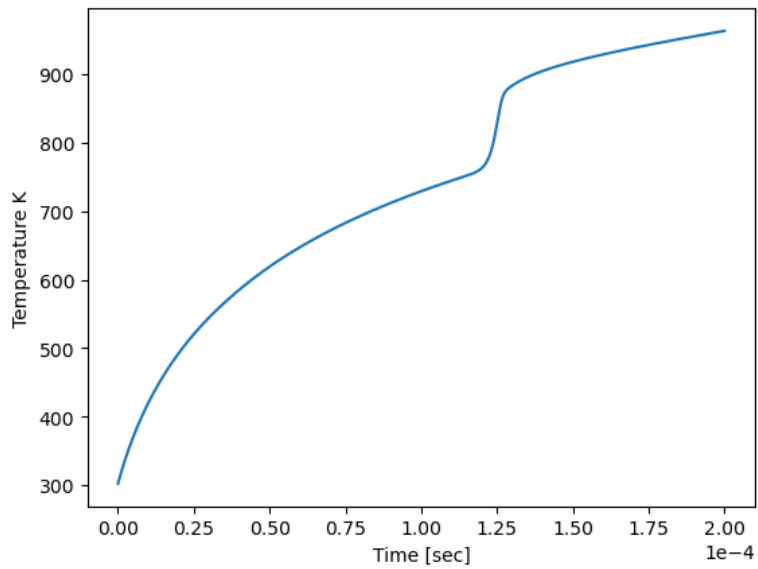


Figure 24: Temperature in the IQT simulation

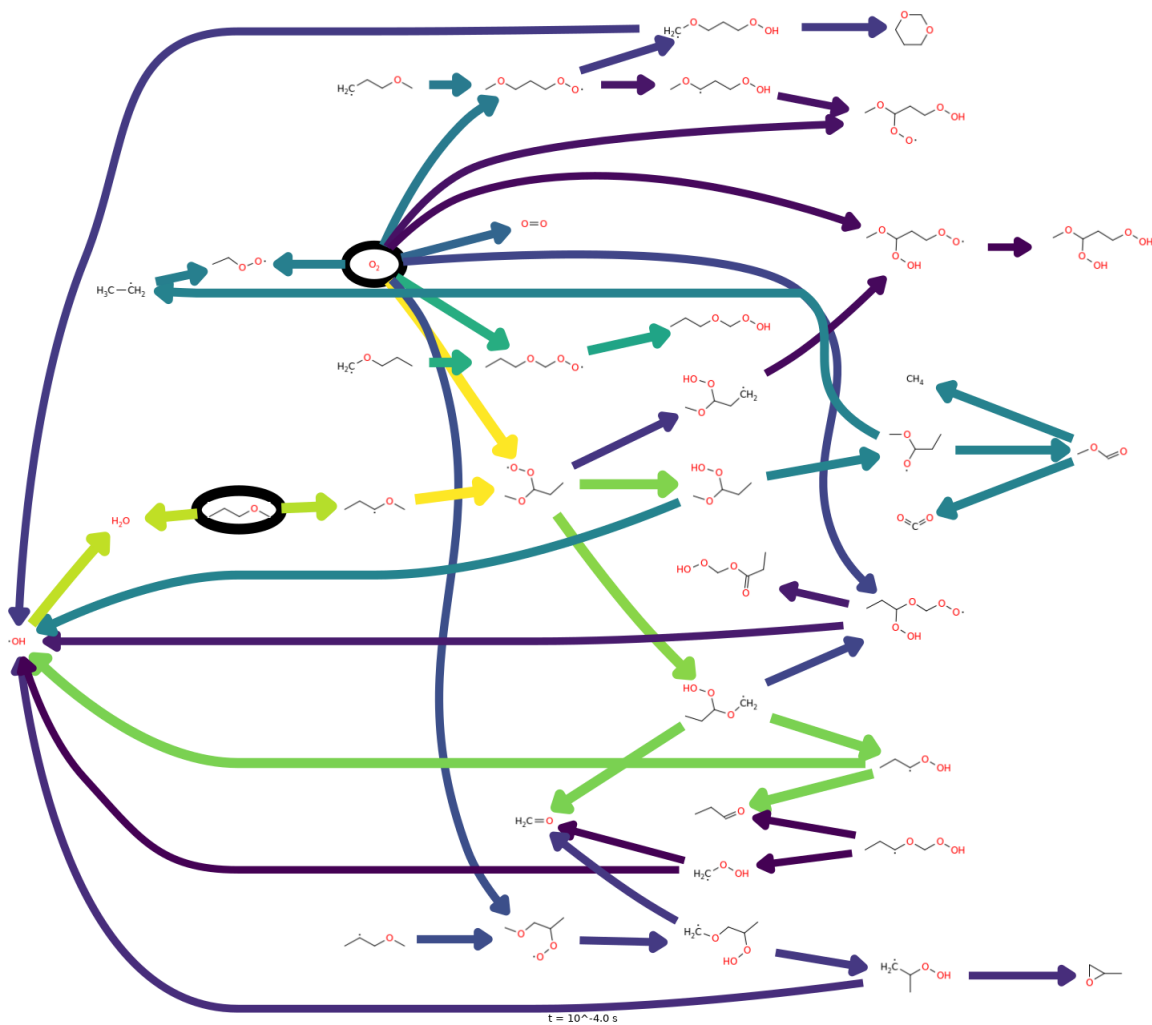


Figure 27: Flux diagram for the IQT simulation at 0.0001 sec.

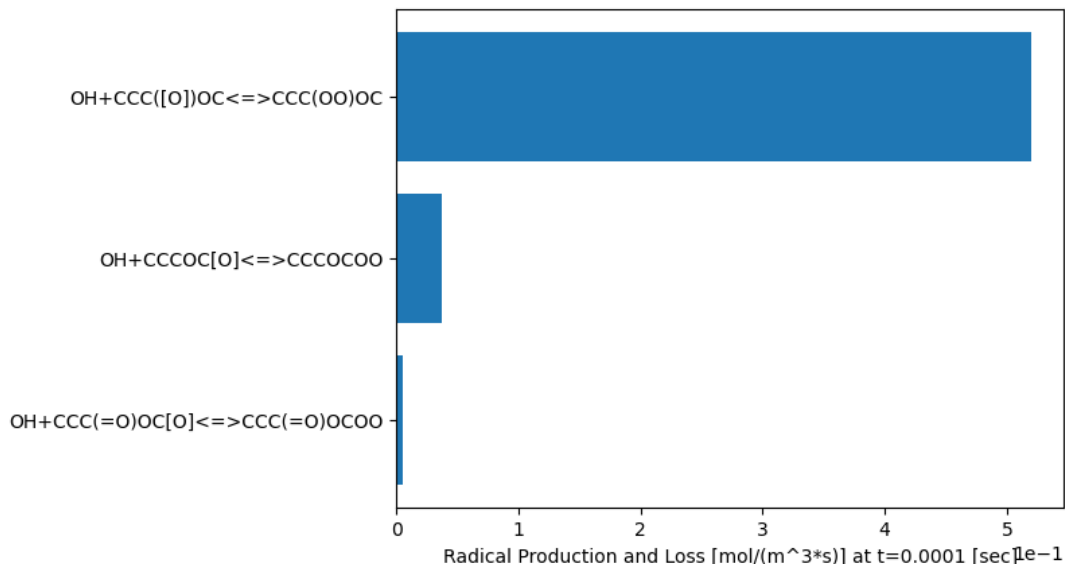


Figure 28: Computed reaction production/loss contributions for all radicals for the IQT simulation at 0.0001 sec.

Figures 29 and 30 show the same plots for the conditions 20 microseconds later, at 0.12 ms, which is the O₂ mole fraction peak, T = 762 K. CCC(OO)OC and CCCOCOO decomposition are still the dominant radical sources. However, at this temperature the ketohydroperoxide feedback loops have turned off as they have become less favorable thermodynamically. The most interesting difference though is the greatly increased concentrations of hydroperoxide species and their radicals approaching ignition.

The chemistry in the IQT at these conditions mostly takes place in a 100 K temperature range and involves similar chemistry to the RCM simulations. However, in the IQT there is a much higher MPE concentration. This causes bimolecular hydrogen abstraction reactions from MPE by larger radicals to become important.

4 Conclusions

This study presents a chemical kinetic mechanism for oxidation and pyrolysis of methyl propyl ether. This kinetic mechanism was constructed iteratively using RMG to generate the model, flux and sensitivity analyses to identify important parameters, improving parameters

with quantum chemistry calculations and literature values and then repeating the cycle. RMG was able to discover almost all of the chemistry on its own, however one important reaction involved an unexpected concerted H shift that would not have been discovered by RMG. We have validated this mechanism against shock tube data at about 10 bar and 1205–1511 K, RCM data at 10–20 bar and 600–900 K and flow tube data at 1 bar and 700–900 K. An analysis of the sensitivities, a list of stationary point geometries, tables of rate and thermochemistry parameters calculated in this study, the associated RMG input file and the full mechanism of 443 species and 26,108 reactions are available in the supporting information.

Methyl propyl ether chemistry is characterized strongly by the reactions branching off and competition between the two main radical addition to O_2 pathways. The two radical pathways transition between addition to O_2 /pyrolysis pathways at significantly different temperatures. This leads to a very high sensitivity to the branching between the two radicals in the flow tube experiments. Low temperature reactivity at higher pressures made it key to simulate the compression stroke when modeling RCM experiments. Competition between the 2nd addition to O_2 and pyrolysis resulted in an abnormally large difference between ignition delay times in the 10 bar and 15 bar simulations at higher temperatures. Under IQT conditions, more representative of diesel engines, the chemistry is similar to that in the RCM except that bimolecular hydrogen abstractions from MPE by peroxy radicals are more important and the ignition timescale is shorter due to the higher MPE concentrations.

This study provides a basis for improving our understanding of detailed ether chemistry across a wide range of temperatures and pressures. It suggests that the branching between pyrolysis and additions to O_2 in key pathways is very important for understanding how easily an ether will ignite.

5 Acknowledgements

The authors thank Dr. Owen Pryor (UCF, currently at Southwest Research Institute, TX) for assistance with shock tube experiments.

This material is based upon work supported by the U.S. Department of Energy's Office of Energy Efficiency and Renewable Energy (EERE) under Award Number DE-EE0007982 (Co-Optima).

The work at UChicago Argonne, LLC, Operator of Argonne National Laboratory, a U.S. Department of Energy Office of Science laboratory, was performed under Contract No. DE-AC02-06CH11357.

This work was authored in part by the National Renewable Energy Laboratory, operated by Alliance for Sustainable Energy, LLC, for the U.S. Department of Energy (DOE) under Contract No. DE-AC36-08GO28308. This research was conducted as part of the Co-Optimization of Fuels Engines (Co-Optima) project sponsored by the U.S. Department of Energy – Office of Energy Efficiency and Renewable Energy, Bioenergy Technologies and Vehicle Technologies Offices. Co-Optima is a collaborative project of several national laboratories initiated to simultaneously accelerate the introduction of affordable, scalable, and sustainable biofuels and high-efficiency, low-emission vehicle engines. Part of this material is based upon work supported by the U.S. Department of Energy's Office of Energy Efficiency and Renewable Energy (EERE) under the Bioenergy Technologies Office (BETO) Program Award Number DE-EE0008726. The views expressed in this article do not necessarily represent the views of the DOE or the U.S. Government. The U.S. Government retains and the publisher, by accepting the article for publication, acknowledges that the U.S. Government retains a nonexclusive, paid-up, irrevocable, worldwide license to publish or reproduce the published form of this work, or allow others to do so, for U.S. Government purposes.

Disclaimer: This report was prepared as an account of work sponsored by an agency of the United States Government. Neither the United States Government nor any agency thereof, nor any of their employees, makes any warranty, express or implied, or assumes any

legal liability or responsibility for the accuracy, completeness, or usefulness of any information, apparatus, product, or process disclosed, or represents that its use would not infringe privately owned rights. Reference herein to any specific commercial product, process, or service by trade name, trademark, manufacturer, or otherwise does not necessarily constitute or imply its endorsement, recommendation, or favoring by the United States Government or any agency thereof. The views and opinions of authors expressed herein do not necessarily state or reflect those of the United States Government or any agency thereof.

The data that supports the findings of this study are available in the supplementary material of this article.

References

- (1) Barrientos, E. J.; Maricq, M. M.; Boehman, A. L.; Anderson, J. E. Impact of Ester Structures on the Soot Characteristics and Soot Oxidative Reactivity of Biodiesel. SAE Technical Papers. 2015.
- (2) Mueller, C. J.; Pitz, W. J.; Pickett, L. M.; Martin, G. C.; Siebers, D. L.; Westbrook, C. K. Effects of oxygenates on soot processes in di diesel engines: Experiments and numerical simulations. SAE Technical Papers. 2003.
- (3) Burger, J.; Siegert, M.; Ströfer, E.; Hasse, H. Poly(oxyethylene) dimethyl ethers as components of tailored diesel fuel: Properties, synthesis and purification concepts. *Fuel* **2010**, *89*, 3315–3319.
- (4) Yanowitz, J.; Ratcliff, M. A.; McCormick, R. L.; Taylor, J. D.; Murphy, M. J. *Compendium of Experimental Cetane Numbers*; 2017.
- (5) Hashemi, H.; Christensen, J. M.; Glarborg, P. High-pressure pyrolysis and oxidation of DME and DME/CH₄. *Combustion and Flame* **2019**, *205*, 80–92.

- (6) Fischer, S. L.; Dryer, F. L.; Curran, H. J. The reaction kinetics of dimethyl ether. I: High-temperature pyrolysis and oxidation in flow reactors. *International Journal of Chemical Kinetics* **2000**, *32*, 713–740.
- (7) Curran, H. J.; Fischer, S. L.; Dryer, F. L. The reaction kinetics of dimethyl ether. II: Low-temperature oxidation in flow reactors. *International Journal of Chemical Kinetics* **2000**, *32*, 741–759.
- (8) Mittal, G.; Chaos, M.; Sung, C. J.; Dryer, F. L. Dimethyl ether autoignition in a rapid compression machine: Experiments and chemical kinetic modeling. *Fuel Processing Technology* **2008**, *89*, 1244–1254.
- (9) Dames, E. E.; Rosen, A. S.; Weber, B. W.; Gao, C. W.; Sung, C. J.; Green, W. H. A detailed combined experimental and theoretical study on dimethyl ether/propane blended oxidation. *Combustion and Flame* **2016**, *168*, 310–330.
- (10) Burke, U.; Somers, K. P.; O’Toole, P.; Zinner, C. M.; Marquet, N.; Bourque, G.; Petersen, E. L.; Metcalfe, W. K.; Serinyel, Z.; Curran, H. J. An ignition delay and kinetic modeling study of methane, dimethyl ether, and their mixtures at high pressures. *Combustion and Flame* **2015**, *162*, 315–330.
- (11) Yahyaoui, M.; Djebaili-Chaumeix, N.; Dagaut, P.; Paillard, C.-E. Ethyl Tertiary Butyl Ether Ignition and Combustion Using a Shock Tube and Spherical Bomb. *Energy & Fuels* **2008**, *22*, 3701–3708.
- (12) Yasunaga, K.; Gillespie, F.; Simmie, J. M.; Curran, H. J.; Kuraguchi, Y.; Hoshikawa, H.; Yamane, M.; Hidaka, Y. A multiple shock tube and chemical kinetic modeling study of diethyl ether pyrolysis and oxidation. *Journal of Physical Chemistry A* **2010**, *114*, 9098–9109.
- (13) Yasunaga, K.; Simmie, J. M.; Curran, H. J.; Koike, T.; Takahashi, O.; Kuraguchi, Y.; Hidaka, Y. Detailed chemical kinetic mechanisms of ethyl methyl, methyl tert-butyl

and ethyl tert-butyl ethers: The importance of uni-molecular elimination reactions. *Combustion and Flame* **2011**, *158*, 1032–1036.

- (14) Danilack, A. D.; Klippenstein, S. J.; Georgievskii, Y.; Goldsmith, C. F. Low-temperature oxidation of diethyl ether: Reactions of hot radicals across coupled potential energy surfaces. *Proceedings of the Combustion Institute* **2020**,
- (15) Ogura, T.; Sakai, Y.; Miyoshi, A.; Koshi, M.; Dagaut, P. Modeling of the Oxidation of Primary Reference Fuel in the Presence of Oxygenated Octane Improvers: Ethyl Tert-Butyl Ether and Ethanol. *Energy & Fuels* **2007**, *21*, 3233–3239.
- (16) Dagaut, P.; Koch, R.; Cathonnet, M. The oxidation of N-heptane in the presence of oxygenated octane improvers: MTBE and ETBE. *Combustion Science and Technology* **1997**, *122*, 345–361.
- (17) Goldaniga, A.; Faravelli, T.; Ranzi, E.; Dagaut, P.; Cathonnet, M. Oxidation of oxygenated octane improvers: MTBE, ETBE, DIPE, and TAME. Symposium (International) on Combustion. 1998; pp 353–360.
- (18) Koroglu, B.; Pryor, O. M.; Lopez, J.; Nash, L.; Vasu, S. S. Shock tube ignition delay times and methane time-histories measurements during excess CO₂ diluted oxy-methane combustion. *Combustion and Flame* **2016**, *164*, 152–163.
- (19) Pryor, O.; Barak, S.; Koroglu, B.; Ninnemann, E.; Vasu, S. S. Measurements and interpretation of shock tube ignition delay times in highly CO₂ diluted mixtures using multiple diagnostics. *Combustion and Flame* **2017**, *180*, 63–76.
- (20) Etz, B. D.; Fioroni, G. M.; Messerly, R. A.; Rahimi, M. J.; St John, P. C.; Robichaud, D. J.; Christensen, E. D.; Beekley, B. P.; McEnally, C. S.; Pfefferle, L. D.; Xuan, Y.; Vyas, S.; Paton, R. S.; McCormick, R. L.; Kim, S. Elucidating the chemical pathways responsible for the sooting tendency of 1 and 2-phenylethanol. *Proceedings of the Combustion Institute* **2020**,

- (21) Kim, Y.; Etz, B. D.; Fioroni, G. M.; Hays, C. K.; St. John, P.; Messerly, R.; Vyas, S.; Beekley, B. P.; Guo, F.; McEnally, C. S.; Pfefferle, L. D.; McCormick, R. L.; Kim, S. Investigation of structural effects of aromatic compounds on sooting tendency with mechanistic insight into ethylphenol isomers. *Proceedings of the Combustion Institute* **2020**,
- (22) Tranchant, J.; Gardais, J. F.; Gorin, P.; Serpinet, J.; Untz, G. Manuel Pratique de Chromatographie en Phase Gazeuse J. Tranchant (Editor), with the collaboration of J. Buzon, N. Guichard, G. Guiochon, J. Lebbe, A. Prevot. Preface by P. Chovin. Paris, Masson et Cie, 1964. 231 pp. — *Journal of Chromatographic Science* — <https://academic.oup.com/chromsci/article-abstract/2/7/13A/330089?redirectedFrom=fulltext>.
- (23) Curtiss, L. A.; Redfern, P. C.; Raghavachari, K. Gaussian-4 theory using reduced order perturbation theory. *Journal of Chemical Physics* **2007**, *127*, 124105.
- (24) Fridlyand, A.; Goldsborough, S. S.; Al Rashidi, M.; Sarathy, S. M.; Mehl, M.; Pitz, W. J. Low temperature autoignition of 5-membered ring naphthenes: Effects of substitution. *Combustion and Flame* **2019**, *200*, 387–404.
- (25) Bourgeois, N.; Goldsborough, S. S.; Jeanmart, H.; Contino, F. CFD simulations of Rapid Compression Machines using detailed chemistry: Evaluation of the ‘crevice containment’ concept. *Combustion and Flame* **2018**, *189*, 225–239.
- (26) Bourgeois, N.; Jeanmart, H.; Winckelmans, G.; Lamberts, O.; Contino, F. How to ensure the interpretability of experimental data in Rapid Compression Machines? A method to validate piston crevice designs. *Combustion and Flame* **2018**, *198*, 393–411.
- (27) Sung, C. J.; Curran, H. J. Using rapid compression machines for chemical kinetics studies. 2014.

- (28) Goldsborough, S. S.; Santner, J.; Kang, D.; Fridlyand, A.; Rockstroh, T.; Jespersen, M. C. Heat release analysis for rapid compression machines: Challenges and opportunities. *Proceedings of the Combustion Institute* **2019**, *37*, 603–611.
- (29) Gao, C. W.; Allen, J. W.; Green, W. H.; West, R. H. Reaction Mechanism Generator: Automatic construction of chemical kinetic mechanisms. *Computer Physics Communications* **2016**, *203*, 212–225.
- (30) Dana, A. G.; Buesser, B.; Merchant, S. S.; Green, W. H. Automated Reaction Mechanism Generation Including Nitrogen as a Heteroatom. *International Journal of Chemical Kinetics* **2018**, *50*, 243–258.
- (31) Chu, T. C.; Buras, Z. J.; Oßwald, P.; Liu, M.; Goldman, M. J.; Green, W. H. Modeling of aromatics formation in fuel-rich methane oxy-combustion with an automatically generated pressure-dependent mechanism. *Physical Chemistry Chemical Physics* **2019**, *21*, 813–832.
- (32) Class, C. A.; Vasiliou, A. K.; Kida, Y.; Timko, M. T.; Green, W. H. Detailed kinetic model for hexyl sulfide pyrolysis and its desulfurization by supercritical water. *Physical Chemistry Chemical Physics* **2019**, *21*, 10311–10324.
- (33) Keçeli, M.; Elliott, S. N.; Li, Y.-P.; Johnson, M. S.; Cavallotti, C.; Georgievskii, Y.; Green, W. H.; Pelucchi, M.; Wozniak, J. M.; Jasper, A. W.; Klippenstein, S. J. Automated computational thermochemistry for butane oxidation: A prelude to predictive automated combustion kinetics. *Proceedings of the Combustion Institute* **2019**, *37*, 363–371.
- (34) Class, C. A.; Liu, M.; Vandeputte, A. G.; Green, W. H. Automatic mechanism generation for pyrolysis of di-tert-butyl sulfide. *Physical Chemistry Chemical Physics* **2016**, *18*, 21651–21658.

- (35) Burke, M. P.; Chaos, M.; Ju, Y.; Dryer, F. L.; Klippenstein, S. J. Comprehensive H₂/O₂ kinetic model for high-pressure combustion. *International Journal of Chemical Kinetics* **2012**, *44*, 444–474.
- (36) Hashemi, H.; Christensen, J. M.; Gersen, S.; Levinsky, H.; Klippenstein, S. J.; Glarborg, P. High-pressure oxidation of methane. *Combustion and Flame* **2016**, *172*, 349–364.
- (37) Benson, S. W.; Golden, D. M.; Haugen, G. R.; Shaw, R.; Cruickshank, F. R.; Rodgers, A. S.; O’neal, H. E.; Walsh, R. Additivity rules for the estimation of thermochemical properties. *Chemical Reviews* **1969**, *69*, 279–324.
- (38) Allen, J. W.; Goldsmith, C. F.; Green, W. H. Automatic estimation of pressure-dependent rate coefficients. *Phys. Chem. Chem. Phys.* **2012**, *14*, 1131–1155.
- (39) Zhou, C. W.; Simmie, J. M.; Curran, H. J. An ab initio/Rice-Ramsperger-Kassel-Marcus study of the hydrogen-abstraction reactions of methyl ethers, H₃COCH₃-x(CH₃)_x, x = 0-2, by .OH; mechanism and kinetics. *Physical Chemistry Chemical Physics* **2010**, *12*, 7221–7233.
- (40) Mendes, J.; Zhou, C. W.; Curran, H. J. Rate constant calculations of H-atom abstraction reactions from ethers by HO₂ radicals. *Journal of Physical Chemistry A* **2014**, *118*, 1300–1308.
- (41) Huynh, L. K.; Ratkiewicz, A.; Truong, T. N. Kinetics of the hydrogen abstraction OH + alkane -H 2O + alkyl reaction class: An application of the reaction class transition state theory. *Journal of Physical Chemistry A* **2006**, *110*, 473–484.
- (42) Jasper, A. W.; Klippenstein, S. J.; Harding, L. B. Theoretical rate coefficients for the reaction of methyl radical with hydroperoxyl radical and for methylhydroperoxide decomposition. *Proceedings of the Combustion Institute* **2009**, *32 I*, 279–286.

- (43) Lu, K. W.; Matsui, H.; Huang, C. L.; Raghunath, P.; Wang, N. S.; Lin, M. C. Shock tube study on the thermal decomposition of CH₃OH. *Journal of Physical Chemistry A* **2010**, *114*, 5493–5502.
- (44) Bossolasco, A.; Faragó, E. P.; Schoemaeker, C.; Fittschen, C. Rate constant of the reaction between CH₃O₂ and OH radicals. *Chemical Physics Letters* **2014**, *593*, 7–13.
- (45) Müller, J. F.; Liu, Z.; Nguyen, V. S.; Stavrakou, T.; Harvey, J. N.; Peeters, J. The reaction of methyl peroxy and hydroxyl radicals as a major source of atmospheric methanol. *Nature Communications* **2016**, *7*, 1–11.
- (46) Farnia, S.; Vahedpour, M.; Abedi, M.; Farrokhpour, H. Theoretical study on the mechanism and kinetics of acetaldehyde and hydroperoxyl radical: An important atmospheric reaction. *Chemical Physics Letters* **2013**, *583*, 190–197.
- (47) Altarawneh, M.; Al-Muhtaseb, A. H.; Dlugogorski, B. Z.; Kennedy, E. M.; Mackie, J. C. Rate constants for hydrogen abstraction reactions by the hydroperoxyl radical from methanol, ethenol, acetaldehyde, toluene, and phenol. *Journal of Computational Chemistry* **2011**, *32*, 1725–1733.
- (48) Yasunaga, K.; Kuraguchi, Y.; Hidaka, Y.; Takahashi, O.; Yamada, H.; Koike, T. Kinetic and modeling studies on ETBE pyrolysis behind reflected shock waves. *Chemical Physics Letters* **2008**, *451*, 192–197.
- (49) Alfazazi, A.; Kuti, O. A.; Naser, N.; Chung, S. H.; Sarathy, S. M. Two-stage Lagrangian modeling of ignition processes in ignition quality tester and constant volume combustion chambers. *Fuel* **2016**, *185*, 589–598.
- (50) Pickett, L. M.; Caton, J. A.; Musculus, M. P. B.; Lutz, A. E. Evaluation of the equivalence ratio-temperature region of diesel soot precursor formation using a two-stage Lagrangian model. *International Journal of Engine Research* **2006**, *7*, 349–370.

- (51) Broadwell, J. E.; Lutz, A. E. A turbulent jet chemical reaction model: NO(x) production in jet flames. *Combustion and Flame* **1998**, *114*, 319–335.
- (52) Johnson, M. S.; Dong, X. ReactionMechanismSimulator. 2020; <https://github.com/ReactionMechanismGenerator/ReactionMechanismSimulator.jl>.